1

Sea ice thickness distribution

Robert Ricker[1], *Luisa von Albedyll*[2] *and Christian Haas*[2]

[1] *NORCE Norwegian Research Centre, Tromsø, Norway*
[2] *Alfred Wegener Institute, Helmholtz Centre for Polar and Marine Research, Bremerhaven, Germany and University of Bremen, Bremen, Germany*

COPYRIGHTED MATERIAL

1.1 Introduction

When discussing the trends and changes in the sea ice cover across the Arctic and Antarctic in the context of global climate change, it is often overlooked that sea ice varies greatly by region and season. This is true not only for the coverage but also for the thickness of sea ice. The regions where sea ice either thins or thickens in a given year can show remarkable fluctuations, and this variability cannot simply be explained by latitudinal radiation or air temperature gradients. For example, the long-term, mean sea ice thickness in the Arctic is characterized by a zonal (i.e. East-to-West) contrast. While thick ice of >4 m is found north of Greenland and the Canadian Archipelago, sea ice north of Siberia is typically much thinner, although located at similar latitude, as shown by satellite-derived maps of ice thickness (Figure 1.1).

The actual spatial distribution of sea ice thickness is strongly governed by the direction and intensity of prevailing winds and ocean currents, which advect the ice, and by atmospheric and oceanic heat fluxes, which show strong regional and temporal variability. Eventually, the geographical distribution of land masses constrains the distribution and extent of sea ice, and together with winds and currents, it also affects the sea ice thickness distribution (ITD) on large scales.

What forms the ITD that we observe on such large scales? Sea ice takes on a variety of complex shapes, unlike a flat surface. Two main processes are responsible for the variability in ice thickness: thermodynamics and dynamics. While thermodynamic growth mostly creates level ice, dynamic, mechanical processes create deformed ice. Winds and ocean currents play a crucial role deep within the interior pack ice zones resulting in drifting sea ice and in turn leading to dynamic alterations in the distribution of sea ice thickness. Figure 1.2 illustrates dynamic changes in ice thickness, showing how ice can thicken or thin over time. Like the variability of winds and currents, ice drift is not consistent but can diverge or converge. Given its relatively thin nature, often just a few meters thick at most, the ice cover easily breaks into smaller floes separated by cracks or leads when in motion. In divergent conditions, leads form, creating open water where new ice develops through thermodynamic growth and thickens. Conversely, in convergent drift, ice floes are pushed together causing collisions. If the forces within the ice become too large, it may break. Then, ice rafting occurs when two sheets of ice just slide over each other without breaking, or ridging occurs when ice fragments and blocks are pushed both onto and beneath the edges of ice floes, forming pressure ridges (as illustrated in Figure 1.2). While rafting

Sea Ice: Its Physics, Chemistry, Biology, Geology and Societal Importance, Fourth Edition. Edited by David N. Thomas.
© 2025 John Wiley & Sons Ltd. Published 2025 by John Wiley & Sons Ltd.

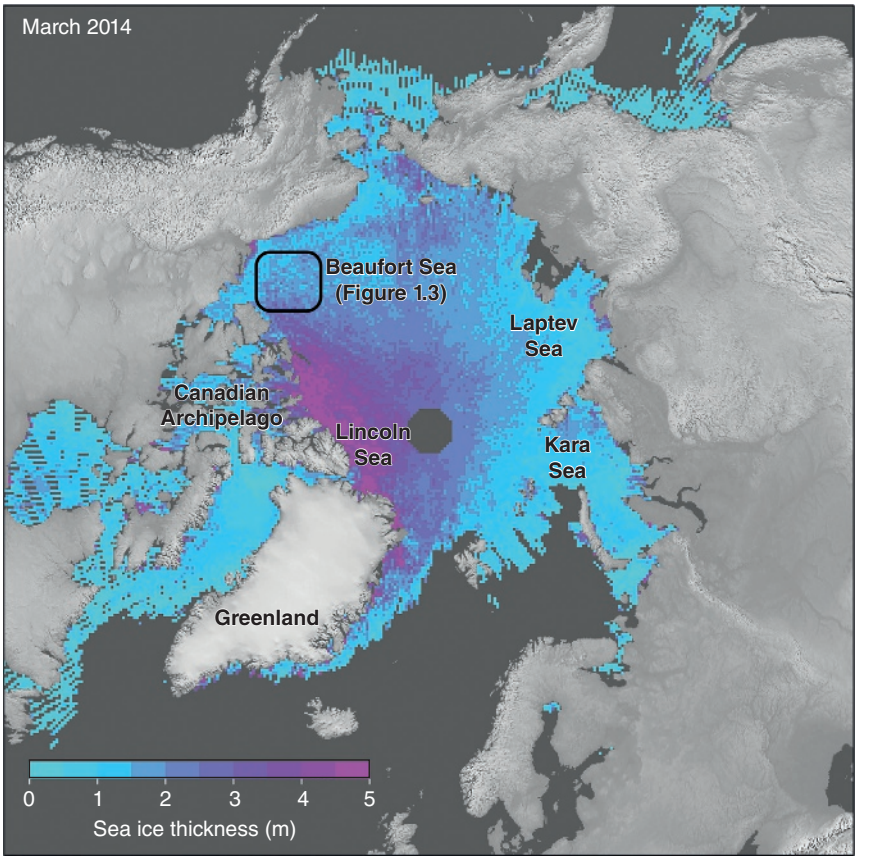


Figure 1.1 Sea ice thickness in the Arctic derived from the European Space Agency satellite CryoSat-2, collected and averaged over one month (March 2014). The black box marks the region where the sea ice thickness profile in Figure 1.3 was measured. Credit: Robert Ricker/CC BY 4.0.

occurs typically in thin ice, pressure ridges are more often formed from thicker ice. Shearing, a special form of deformation, can cause rupture zones creating both leads and pressure ridges. Naturally, these dynamically formed ridges are significantly thicker than the adjacent, thermodynamically grown, undeformed level ice.

Dynamic and thermodynamic growth and decay together shape the ITD that is often displayed as a histogram of the different sea ice thickness categories present in a region. Figure 1.3 displays a thickness profile that showcases the effects of dynamic and thermodynamic processes on the distribution of ice thickness. This specific example is drawn from the Canadian Beaufort Sea (see Figure 1.1) and was captured during a westward aerial survey originating from the northwest corner of Banks Island. The profile begins above a recurring coastal polynya, where new ice measures less than 0.5 m in thickness. It then crosses thicker first-year ice (FYI), at 1.2 m in thickness, which had previously formed in the polynya and has been exported from there. Finally, the profile ends above ice exceeding 2 m in thickness, consisting of old multiyear ice (MYI) originating from the high Arctic Ocean and Canada Basin. This latter ice is characterized by extensive deformation with numerous pressure ridges measuring over 6 m in thickness. In this example we also see that the thick

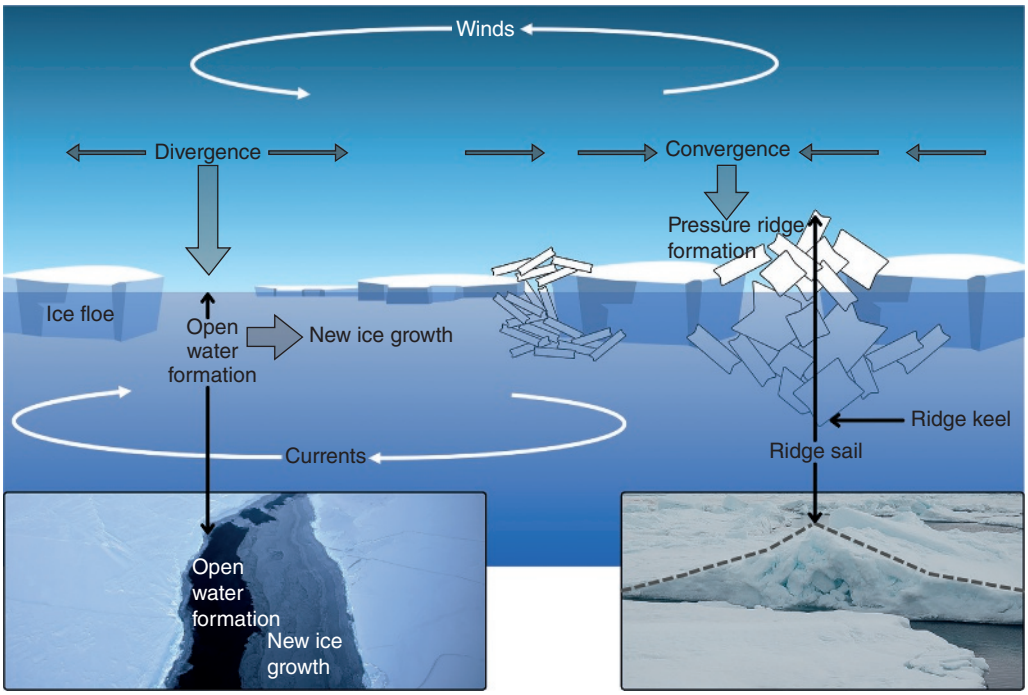


Figure 1.2 Illustration of the different dynamic and thermodynamic processes contributing to the development of the sea ice thickness distribution. *Source*: Meier & Haas (2011)/Arctic Monitoring and Assessment Programme. Bottom left photo: Michael Gutsche/Alfred-Wegener-Institute/CC BY 4.0, bottom right photo: Evgenii Salganik/CC BY 4.0.

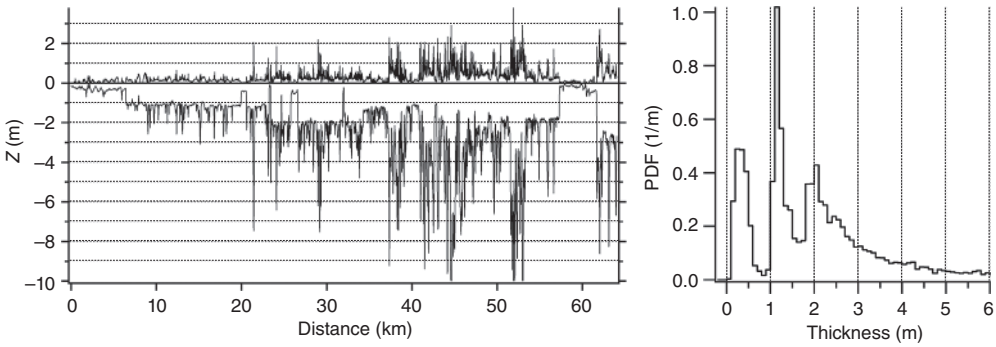


Figure 1.3 Sea ice thickness profile and thickness distribution (probability density function, PDF, 0.1 m bin width) from the Canadian Beaufort Sea obtained by airborne electromagnetic (EM) profiling (see Figure 1.1). The 65-km-long profile was surveyed on 19 March 2014, and which extends from the northwest corner of Banks Island (left) to approximately 73°33′N, 127°29′W (right). Positive *Z* shows surface height profile obtained from laser altimetry, while negative *Z* shows EM ice thickness.

ice cover is interrupted by refrozen leads of varying thicknesses and widths, resulting from widespread divergent ice motion in this region.

Due to the interplay of the various ice growth and deformation processes, the resulting ITDs can be quite complex (Figure 1.3). However,

the amount and thickness of deformed and level ice bear information about the integrative formation processes having contributed to the thickness distribution at any given time and location. It is, therefore, important to be able to observe different ice thickness classes (from thin to thick ice) with high spatial resolution and to take their importance for sea ice processes into account.

We will discuss the strong variability in sea ice thickness on all scales from regional differences between, e.g. the coasts of Canada and Greenland and the Siberian Shelf, to small-scale variability of pressure ridges (up to 20 m) and of leads covered with thin ice (several centimeters).

In Section 1.2 we will lay the foundational understanding of the ITD, before we will explore methods used to gauge sea ice thickness (Section 1.3). There, we will also explore the challenge of accurately describing the ITD across different scales, from very confined areas to the vast polar regions, considering the substantial variability between areas where various ice growth processes may prevail.

Eventually, we will examine the global ITD (Section 1.4) and related changes and trends (Section 1.5). In Section 1.6, we will take a look into recent advances and how we can use emerging technologies to improve our understanding in this field.

1.2 The sea ice thickness distribution

1.2.1 Statistical description

The interaction between dynamic and thermodynamic processes leads to substantial variations in ice thickness, ranging from a few centimeters to several meters (Wadhams, 2000). Given that most air–ice–ocean interactions and biogeochemical processes are particularly influenced by specific ice thickness ranges, such as very thin ice or thick ridges, knowledge of the relative coverage of different ice thicknesses is essential for the parameterization of important climate processes (Holland et al., 2006; Lipscomb et al., 2007; Notz, 2009). The broad spectrum of ice thicknesses can be effectively summarized through an ITD, a histogram characterizing the likelihood of encountering ice of a particular thickness. Mathematically, the ITD (denoted as $g(h)$) can be expressed as a probability density function in the following form (Thorndike et al., 1975):

$$g(h)\ dh = dA(h,\ h + dh)/R \tag{1.1}$$

where $dA(h,\ h + dh)$ represents the fractional area of a region, denoted as R, covered by ice with thickness ranging from h to $(h + dh)$. In practice, the thickness distribution is primarily acquired along linear profiles, and thus, both dA and R are one-dimensional, with R representing the total length of the profile. The numerical values associated with each thickness bin are divided by the corresponding bin width (dh) and expressed in units of m^{-1}. Thus, being independent of the bin width, the ITD facilitates meaningful comparisons among thickness distributions obtained from various surveys.

When compiling representative sea ice thickness measurements into an ITD, the shape of the ITD reveals the interplay between thermodynamic and dynamic forces on the sea ice since its formation.

Typical ITDs are characterized by one or two modal peaks and a long tail (Haas et al., 2010; Rack et al., 2021; Sumata et al., 2023). Consequently, the ITD is not symmetrical but positively skewed, meaning that thinner ice is more common than thicker ice. Since thermodynamic growth leads to a regionally almost homogeneous ice thickness, the most frequent ice thickness, i.e. the mode, is often associated with the thermodynamically grown, undeformed, level ice (Thorndike, 1992a; Wadhams, 1994; Haas et al., 2008; Albedyll et al., 2022). For example, the two modes in Figure 1.3 represent the thermodynamic thickness of the younger ice that formed within the last growth season (FYI) and the older ice that

has survived at least one summer (MYI). The MYI mode is often broader than the FYI mode because every thermodynamic cycle slightly increases the spread of the ice thicknesses distribution (Hansen et al., 2013). Sea ice deformation introduces the skewed shape of the ITD by creating a long tail that consists of the crests and flanks of pressure ridges. For some applications, open water is included in the ITD in the smallest bin fraction. Various statistical measures describing the mode and tail of the ITD are used to interpret the ice regime. The width of the mode of the distribution can be described by the *full width at half maximum* (FWHM). A small FWHM and a high *modal peak* indicate a narrow and prominent mode typical for younger and thinner and more uniform ice regimes (Rabenstein et al., 2010; Albedyll et al., 2022; Sumata et al., 2023). In contrast, the *variance* of the ITD describes the spread of observed thickness values. Large variance is indicative of large fractions of deformed ice (e.g. Sumata et al., 2023). Deformed ice is often defined as the portion of sea ice exceeding the maximum theoretical thickness of thermodynamically grown ice, typically in the range of 3–5 m (e.g. Rack et al., 2021; Albedyll et al., 2022). The tail of the ITD can be reasonably well approximated using a *log-normal, exponential*, or *power-law* function that begins at a cut-off value, often corresponding to the dominant mode (Wadhams, 1994; Flato & Hibler, 1995). The *slope of the tail*, characterized by, for instance, the e-folding of the exponential function, has also been found to be indicative of the deformation regime (Rabenstein et al., 2010; Albedyll et al., 2021).

A typical icescape comprises extensive areas of level ice interrupted by distinct vertical morphological features like pressure ridges, rafts, and leads. When categorizing level ice, a minimal vertical thickness gradient is used as a criterion (Wadhams & Horne, 1980; Rabenstein et al., 2010). Pressure ridge sails and keels are considered local maxima and minima in the ice surface or draft profile, provided they exceed a specified cutoff height. Independent ridges and keels are identified if they meet the Rayleigh criterion, i.e. they must be separated by a data point of more than half their height to be considered as separate features (Wadhams & Davy, 1986). In open or refrozen leads and cracks, sea ice thickness drops to zero or very thin, level thicknesses, respectively. Statistical properties of ridges and leads, such as their frequency or size, often follow simple exponential or log-normal distributions (Wadhams, 2000; Rabenstein et al., 2010; Tan et al., 2012; Muchow et al., 2021). Some applications concentrate on the surface rather than the total thickness. They describe the surface roughness using metrics like the mean profile height, the standard deviation of profile elevation differences from the mean (rms height), an exponential normal function, and the autocorrelation length (Saldern et al., 2006; Duncan & Farrell, 2022). Information about the surface roughness and sail heights is required for the estimation of drag coefficients. These drag coefficients control air–ice interactions in the momentum balance equation describing the ice motion in sea ice models (Castellani et al., 2014; Mchedlishvili et al., 2023; Krumpen et al., 2025).

1.2.2 Processes changing the ice thickness distribution

Thermodynamics and dynamics change ice thickness on different spatial and temporal scales. The associated temporal changes of the ITD is defined as "g" (Thorndike et al., 1975):

$$\partial g/\partial t = -\partial(fg)/\partial h - div(vg) + \phi \qquad (1.2)$$

Three terms contribute to this equation (as illustrated in Figure 1.4): $f(h,x,t) = dh/dt$ is the thermodynamic growth or melt rate of ice of thickness h at a location x and time t. Those processes are active on synoptical scales of 1000 km and seasonal timescales. The ice advection $div(vg)$ describes the convergence and divergence of the ice where

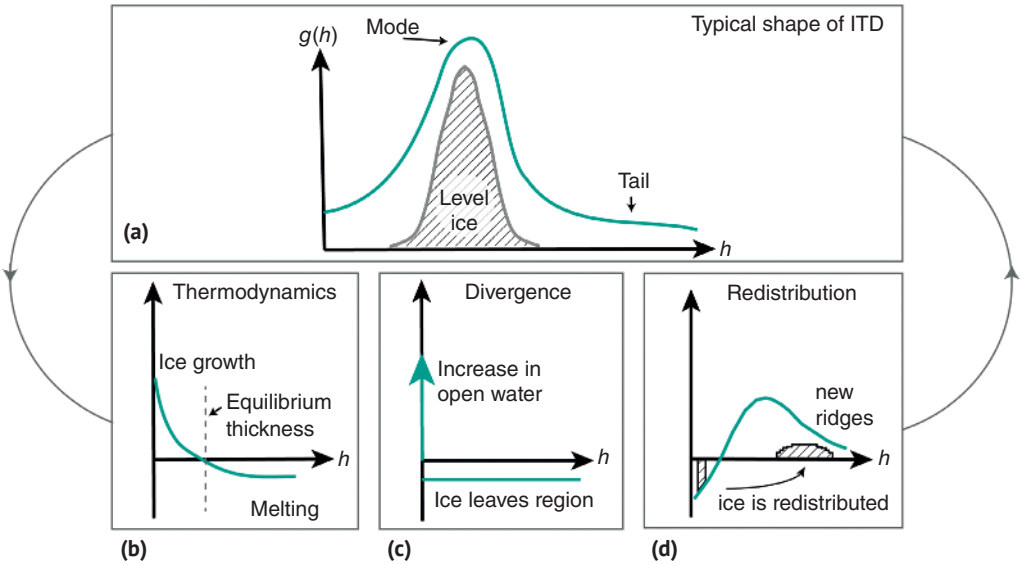


Figure 1.4 (a)–(d) Illustration of the contribution of the different processes changing the sea ice thickness distribution given in Eq. (1.2). *Source*: Thorndike et al. (1992b)/John Wiley & Sons.

v is the drift velocity vector. Since the sea ice velocity varies on temporal and spatial scales of a few hours and hundreds of meters, this term leads to much more abrupt changes in ice thickness than thermodynamics. The same applies to the subsequent redistribution of the ice from thinner to thicker ice classes in case of convergence, which is described by ϕ, the so-called redistribution function (Lipscomb et al., 2007).

Thermodynamics

Since atmospheric and oceanic forcing of thermodynamic growth and melting mostly varies on synoptic scales spanning up to 1000 km, thermodynamic growth and melting alter the ice thickness on these larger, regional scales. The rate of thermodynamic growth and melting ($f(h, x, t) = dh/dt$) is determined by the conductive heat transfer between the ocean and the atmosphere. Consequently, f depends on the temperature gradient and the thermal conductivity of the ice, which is influenced by its microstructure, including the presence of brine and air (Petrich & Eicken, 2017).

Ice growth: Sea ice grows at its bottom when the water is at its salinity-dependent freezing point and when the heat flux through the ice exceeds the heat flux from the water below (Petrich & Eicken, 2017). Initially, in open water, thermodynamic growth is rapid, but gradually, it slows down as thicker ice results in less efficient heat transfer. Eventually, the ice reaches an equilibrium thickness, where it stops growing because the inefficient heat transport becomes balanced by the ocean heat flux from below (Maykut, 1986). The presence of snow further limits heat transport through the ice, as its thermal conductivity, typically ranging between 0.11 and 0.35 W m^{-1} K^{-1} (Chapter 2; Massom et al., 2001), is much smaller than the sea ice's heat conductivity. As a result, the presence of snow significantly slows down ice growth and reduces the equilibrium ice thickness.

Ice melt: Melting reduces the average ice thickness and shifts the thickness distribution left toward thinner ice, as illustrated in Figure 1.4. Therefore, the ITD is closely tied to the summer ice extent defined by the isoline of zero ice thickness. When the amount of ice melt during the

summer exceeds the modal thickness, substantial regions become ice-free. During the summer, ice is melted by solar and infrared radiation as well as atmospheric heat, both at the surface and internally. In contrast, bottom and lateral melting can occur at any time when the ocean heat flux to the ice exceeds the conductive heat flux through the ice to the atmosphere, i.e. when the ice is thicker than its equilibrium thickness. This is particularly common in thicker ice such as pressure ridges. Consequently, bottom melting can even occur during the winter, resulting in a negative change in the ITD, as depicted in Figure 1.4b. Melt rates depend critically on the ITD itself (e.g. Perovich et al., 2003). Pressure ridges experience faster melting during the summer for several reasons (e.g. Salganik et al., 2023). First, the heat flux through thick ice is lower. Second, pressure ridge keels protrude far down into the water, potentially reaching into warmer water. Third, ridge keels increase the roughness of the ice underside, and thus the upward turbulent ocean heat fluxes (Amundrud et al., 2006; see Chapter 8 for more details). And last, the flanks of ridge sails are exposed more normally to the incident solar radiation than ridge crests, as solar elevation is low in polar regions. Although the variations of melt rates might seem to be rather small, they can contribute to significantly different thickness changes during the ablation season. When snow and ice melt, the melt water tends to collect in topographic depressions, forming melt ponds. Even small amounts of snowmelt can have a significant impact on the surface albedo. Typical surface broadband shortwave albedos are 0.8–0.85 for dry snow, 0.7–0.8 for wet snow, 0.6–0.7 for bare ice, and 0.1–0.5 for melt ponds (Chapter 3). Once formed, melt ponds absorb more solar radiation than adjacent snow or bare ice, thereby increasing local melt rates. Throughout the summer, the surface of melt ponds lowers until it is at sea level, leaving vertical pond walls that reach deep into the ice. This positive feedback causes significant changes to the ITD of level ice, and it contributes to an increase in surface roughness (e.g. Polashenski et al., 2012; Landy et al., 2014).

Advection and divergence

Advection and divergence act on all spatial scales from a few meters to basin-wide scales. The term "ice advection" ($\mathrm{div}(vg)$) quantifies changes in ice thickness resulting from the movement of ice at a specific velocity (v) and with a particular thickness distribution (g). In a Eulerian framework, i.e. observing a fixed geographical area, the advection term quantifies the net influx or outflux of ice into or out of that area. Returning to our earlier discussion on the large-scale regional thickness gradients in the Arctic (Section 1.1), ice advection accounts for these differences that cannot be explained by thermodynamics. Ice is transported away from the Siberian shelf, which results in large-scale divergence ($\mathrm{div}(vg) > 0$) and small ice thicknesses there. Conversely, along the north coasts of Canada and Greenland, ice is advected toward the land, which leads to convergence ($\mathrm{div}(vg) < 0$) and thicker ice. In a Lagrangian framework, where we follow the motion of the ice itself, the ice advection term induces changes within the study area rather than the ice flux through the boundaries of a fixed grid. In this context, the advection term can be simplified as $\mathrm{div}(vg) = g\ \mathrm{div}(v)$ (Thorndike, 1992a). The Lagrangian reference system offers the advantage of being able to study the same ice without any external ice being gained or lost. In this case, convergence and divergence of a region are directly linked to thickness changes (Albedyll et al., 2022).

Divergence causes cracks, leads, or polynyas, resulting in open water areas where new ice can form. Consequently, in a given region, divergence removes ice of a finite thickness, causing a distinct shift in the thickness distribution, often depicted as a delta pulse at zero thickness (see Figure 1.4c).

Redistribution during convergence

Redistribution shapes the ice thickness on local scales of decimeters to meters. The redistribution function (ϕ) describes how sea ice thickness changes within an area due to sea ice deformation. This function summarizes all

mechanical processes, such as ridging, rafting, and open-water formation, that change the relative occurrence of different thicknesses but do not influence the mean thickness. The redistribution function is proportional to the magnitude of the deformation, i.e. how much ice area was gained (divergence) or lost (convergence). In addition, ϕ depends strongly on the mechanical reaction of ice toward the applied stress. Those mechanical properties are not precisely known as they depend on small-scale ice properties like ice porosity and impurities and large-scale ice pack properties like snow cover and weaknesses caused by previous deformation events. Therefore, sea ice mechanics is the subject of current research with different ice strength parameterizations, rheologies, and yield curves used in sea ice modeling prescribing the mechanical behavior of sea ice (see Section 1.2.3; Thorndike et al., 1975; Rothrock, 1975; Hibler, 1979; Lipscomb et al., 2007; Ringeisen et al., 2023). Chapter 4 provides an in-depth discussion of the ice engineering view on breaking ice. Since ice strength depends on ice thickness, we expect that thinner ice deforms more easily than thick ice. Thus, convergence closes open-water areas first and then transforms thin ice into thicker ice classes. This reduces the presence of open water and thin ice and increases the occurrence of thicker ice (Figure 1.4d). Commonly, it is assumed that only a small fraction (e.g. 15%) of the ice participates in the deformation (Thorndike et al., 1975). Several different parameterizations based on studies like Thorndike et al. (1975) and Lipscomb et al. (2007) are available to describe this general behavior of ice redistribution. There are promising attempts to constrain parts of the redistribution function based on conceptual models (e.g. Hopkins et al., 1991, 1999; Hopkins, 1994, 1998; Roberts et al., 2019), three-dimensional discrete-element-method simulation tools (Muchow & Polojärvi, 2024), tank experiments (Tuhkuri & Lensu, 2002), and high-resolution observations (Vinje et al., 1998; Amundrud et al., 2004; Albedyll et al., 2022). Pan-Arctic, high-resolution ITDs, provided by the altimeter on the ICESat-2 satellite, will most likely advance this open field of research (Duncan & Farrell, 2022).

The ITD is both a prerequisite for and a consequence of thermodynamics and dynamics. Each of these processes influences the ITD in distinct ways, as depicted in Figure 1.4. Changes in ice thickness often result from the interplay of these processes, with mutual influences on each other.

For instance, divergence creates open water, reducing the ice thickness. When freezing conditions prevail, new ice rapidly forms through thermodynamic processes in the open water, increasing the overall ice volume. However, this newly formed, thinner ice is mechanically weaker, making it susceptible to being ridged during subsequent convergence events. This leads to the transformation of initially thin ice into thicker ridges. In contrast, during melting conditions, the open water created by divergence absorbs more sunlight and the fractured ice pack is prone to stronger melting (Perovich et al., 2001; Arntsen et al., 2015; Hwang et al., 2017; Lei et al., 2020). Hence, any interpretation or prediction regarding changes in the distribution of ice thickness concerning climate change must consider both thermodynamic and dynamic processes, as well as any feedback mechanisms associated with them.

1.2.3 Implementation in sea ice models

Sea ice models are essential components of Earth System Models (ESMs) that are capable of simulating the physical, chemical, and biological processes in the atmosphere, ocean, land, and sea ice that govern the evolution of Earth's climate (Chapter 10). These numerical *climate models* are crucial for climate prediction and understanding climate feedback mechanisms. Here we give a brief summary of how sea ice thickness change is implemented in sea ice models and refer

the interested reader to Chapter 10 for more details on ESMs.

Sea ice models are formulated as expressions of local conservation of momentum, mass, and heat, which are driven through various underlying thermodynamic and dynamic processes (see Section 1.2.2). Thermodynamic processes control melting, freezing, and dissolution, involving processes like solar and longwave radiation absorption, thermal conduction, and brine convection. They are controlled by the surface energy balance:

$$F_{\mathrm{SW,\,net}} + F_{\mathrm{LW,\,net}} + F_{\mathrm{sens}} + F_{\mathrm{lat}} + F_{\mathrm{m}} - F_{\mathrm{cond}} = 0 \tag{1.3}$$

The individual contributions are the net shortwave and longwave radiation ($F_{\mathrm{SW,\,net}}$ and $F_{\mathrm{LW,\,net}}$, respectively), the sensible and latent heat flux (F_{sens} and F_{lat}, respectively), heat used for melting (F_{m}), and the conductive heat flux (F_{cond}) through the ice. See Chapter 10 for details.

Dynamic processes control the advection and deformation of sea ice leading to a redistribution of thickness from an Eulerian perspective.

On a regional scale, the large-scale spatial thickness distribution is obtained by solving a force balance equation considering the main forces acting on a unit area of the sea ice cover:

$$Ma = \tau_{\mathrm{a}} + \tau_{\mathrm{w}} + F_{\mathrm{C}} + F_{\mathrm{i}} + F_{\mathrm{t}} \tag{1.4}$$

where a sea ice element of mass M accelerates with a according to the sum of the air and water drags τ_{a} and τ_{w}, the Coriolis force F_{C}, internal ice forces F_{i}, and of the force due to sea surface tilt F_{t}. Typically, the first two terms are dominant by more than an order of magnitude. The mean ice thickness for each model grid cell is determined by solving Eq. (1.4), which accounts for ice motion, and distributing the drifted ice volume equally across the cell area, under the assumption of mass conservation as discussed in Chapter 10. As for the redistribution term in Eq. (1.2), considering ice strength and rheology to realistically simulate sea ice deformation is crucial here. The mechanical processes associated with the consequences of convergence and divergence are not explicitly resolved on the scale of individual floes breaking in sea ice models but parameterized by describing the changes of the ITD (see Section 1.2.2). While simple models have just one ice thickness class, meaning that they allow only a uniform thickness within a given grid cell, more complex models better reflect the dynamic processes by including a set of ice thickness classes describing the ITD (Section 1.2.1). This differentiation allows for changing the frequency of occurrence of different ice classes after the deformation events (see "redistribution during convergence" above). The exact parameterization of dynamic processes is still a field of research and has a significant impact on the model mean state (Ungermann et al., 2017; Massonnet et al., 2019).

Pressure ridges and leads form large-scale systems of so-called linear kinematic features (LKFs).

Elasto-brittle sea ice models like nextSIM (Rampal et al., 2016) have the capability to simulate sea ice deformation more realistically, and compared to other sea ice models, they simulate a greater number of LKFs and more refined LKFs as the spatial resolution is increased (Mehlmann et al., 2021). LKFs can be observed and quantified by high-resolution satellite remote sensing, e.g. by synthetic aperture radar images (e.g. see Chapter 5; Hutter et al., 2019; Itkin et al., 2023; von Albedyll et al., 2024). Extensive deformation datasets derived from the RADARSAT Geophysical Processor System (RGPS), which uses radar data from the Canadian RADARSAT satellite mission, have been used as a reference to benchmark models in their ability to resolve LKFs and to reproduce their statistical properties (Hutter et al., 2019, 2022). How well models can resolve LKFs also depends on the choice of the model grid and its discretization (Mehlmann et al., 2023).

In the future, it will be important to better understand sea ice deformation processes with the help of field experiments like Multidisciplinary Drifting Observatory for the Study of Arctic Climate (MOSAiC) and

coincident high-resolution satellite data like from Ice, Cloud and Land Elevation Satellite 2 (ICESat-2), to eventually improve the implementation of such processes in sea ice models.

1.3 Measurement techniques on different scales

In this section, we present ice thickness observation methods, with a view on how the full ITD can be measured across different scales. The accuracy and insights obtained from these measurements are directly influenced by the scale of observation employed. Indeed, whether we utilize on-ground techniques or satellite-based methodologies with different spatial resolutions, the resultant data will invariably differ, contingent upon the detection of both small- and large-scale sea ice features.

While sea ice extent and concentration can be measured with sufficient accuracy by satellites from space (Chapter 5), determining its thickness is much more difficult, even from aircraft or while standing on the ice. On the one hand, we must infer information from below the water's surface, while on the other hand, the relative thinness and complex topography of the sea ice pose significant challenges for geophysical measurement techniques. Therefore, most methods are indirect measurements, which observe ice properties closely related to ice thickness. This chapter briefly presents the most important submarine, on-ice, and airborne ice thickness measurement methods (Figure 1.5). For completeness, we also summarize spaceborne ice thickness measurements and direct the interested reader to Chapter 5 for more details.

One important difference between spaceborne and airborne or on-ground ice thickness observations discussed in this chapter is that the latter two can usually provide information about the actual thickness distribution, while spaceborne methods typically obtain large-scale mean thickness information. However, this is changing with current and future satellite missions that are or will be able to resolve spatial

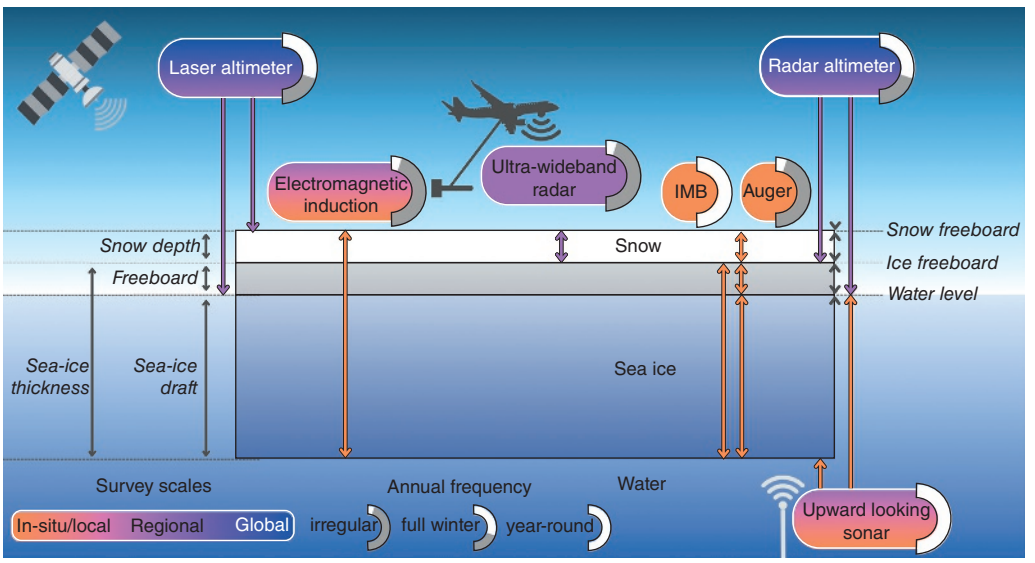


Figure 1.5 Ice floe cross-section showing definitions of ice and snow thickness terms and parameters, and primary measurement techniques to observe different sea ice and snow parameters on various temporal and spatial scales.

variability on much smaller scales (e.g. ICESat-2, Copernicus Polar Ice and Snow Topography Altimeter [CRISTAL]; see Section 1.6 and Chapter 5). The methods discussed here are important for revealing the underlying processes of observed thickness variability across different spatial and temporal scales. As each method has its own limitations in terms of accuracy as well as spatial and temporal coverage, we need the combination of different observation techniques for a full characterization of the ITD. For example, auger drillings provide very accurate and precise thickness measurements, but only for a very small area and for a limited period of time, depending on the accessibility of the ice. On the other hand, satellite observations work year-round, covering the entire Arctic, but have much larger uncertainties.

1.3.1 Local/*in situ* measurements

Drill-hole measurements

Drill-hole measurements using augers provide the most direct and most accurate ice thickness information (e.g. Haas & Druckenmiller, 2009). They are the only method allowing the simultaneous observation of all important components of ice thickness, namely the thickness of both ice and snow, as well as ice draft and freeboard (the depth of the ice underside below the water level and the height of the ice-surface above the water level, respectively) with one measurement (Figure 1.5). However, drill-hole measurements are slow and tedious and require access to the ice, such that their spatial extent and statistical representativeness can be quite limited and usually does not include information about very thin or thick ice due to logistical reasons. Nevertheless, they can provide important information on key aspects of the ITD, e.g. modal thickness representing the thickness of the most frequently occurring, thermodynamically grown level ice (Eicken et al., 1995; Worby et al., 1996). It is also good practice to support measurements made by other means with a few drill-hole measurements for calibration and/or validation.

Ice mass balance buoys

Ice mass balance buoys (IMBs) are essential tools for monitoring sea ice thickness (Richter-Menge et al., 2006; Jackson et al., 2013; Perovich et al., 2023). They are deployed on drifting sea ice, typically during research cruises, and measure changes in ice thickness autonomously, providing real-time data over time that are transmitted by satellite communication systems.

IMBs measure both the freezing and melting processes above and below the ice. They use thermistor strings or acoustic sensors to track changes in the ice surface and bottom, providing data on snow depth, ice growth, and melt rates. This information is crucial for understanding the seasonal evolution of sea ice. However, similar to drill-hole measurements, thickness data from buoys are limited to their immediate location on the drifting ice floe and may be strongly affected by the presence of local snow drifts, for example.

Visual observations

Ice thickness can also be observed visually by recording ice floes broken by an icebreaker. The broken ice fragments are often moved side-up against the ship's hull, revealing their cross profile. Coordinated, systematic visual ice observations are encouraged by the international Antarctic Sea Ice Processes and Climate (ASPeCt) program and have been compiled by Worby et al. (2008) to provide a unique snapshot of circum-Antarctic sea ice thicknesses.

1.3.2 Regional-scale observations

Ground-penetrating radars

With ground-penetrating radar (GPR), the travel time of radar waves between the radar instrument and reflections from the snow surface, snow–ice interface, or ice–water interface is measured. GPR could, therefore,

potentially yield coincident measurements of snow and ice thickness (Haas & Druckenmiller, 2009; Galley et al., 2009). While radar frequencies of a few 100 MHz have to be used to penetrate through the sea ice, higher frequencies ≥1 GHz have to be used to resolve the much thinner snow. Although the references above include few examples of successful point measurements, widespread application of the method suffers from highly variable dielectric ice properties due to variations in brine volume, brine distribution, and other internal interfaces. These lead to highly variable radar propagation speeds and radar absorption, such that acquired radargrams can be difficult to interpret. Recent new technology developments have led to the design of ultra-wideband, frequency-modulated, continuous-wave (FMCW) radars for snow depth measurements over sea ice (Panzer et al., 2013). These are now routinely flown for snow thickness surveys over Arctic and Antarctic sea ice (Kurtz et al., 2013; Jutila et al., 2022a).

Submarine and moored upward-looking sonars

A substantial amount of ice thickness data have been obtained by means of upward-looking sonars (ULSs), also called ice profiling sonars. These have been mounted either on military nuclear submarines (e.g. Bourke & Garrett, 1987; Rothrock et al., 2008; Sumata et al., 2023) or on oceanographic moorings (e.g. Vinje et al., 1998; Melling et al., 2005; Behrendt et al., 2013; Hansen et al., 2013; Krishfield et al., 2014) and have provided some of the most extensive and invaluable information of long-term ice thickness variability and change since the 1950s (Figure 1.6).

With this method, estimates of ice draft, the depth of the ice underside below the water level, are obtained, serving as a reliable proxy for ice thickness. The instruments measure the travel time, t, of a sonar pulse transmitted by the ULS and reflected back from the ice bottom (Figures 1.5 and 1.6). Additionally, the depth of the sonar beneath the water level, z, and the sound velocity, c, in the water must be known. Then, ice draft, d, is calculated according to

$$d = z - c * t/2 \tag{1.5}$$

The depth of the ULS is derived from pressure sensors, whose measurements are also dependent on atmospheric sea level pressure. The sound velocity profile is either assumed constant with a certain sound speed or taken from sea-water conductivity, temperature, and depth measurements or a mixed layer model (Behrendt et al., 2013). Measurements are also corrected for sonar tilt which can be caused by currents. Data processing can become quite complicated in the case of strong water stratification or when the measurements are performed close to ocean frontal zones. A plausibility test for the depth measurement or the sound velocity profile can be performed when profiling the water level in open leads. There, the measured sonar distance must equal the ULS depth.

Sea ice thickness, h, is calculated from draft, d, by assuming isostatic equilibrium, a certain snow depth, zs, and water, ice, and snow densities ρw, ρi, and ρs:

$$h = (\rho w\, d - \rho s\, zs)/\rho i \tag{1.6}$$

Overall, uncertainties of sound velocity profiles, biases due to sonar beam divergence, and other technical issues lead to draft uncertainties in the range between 0.10 (Melling & Riedel, 1995) and 0.25 m (Rothrock & Wensnahan, 2007). Accuracies have improved with the use of high pulse repetition rates, which allow better detection of leads between ice floes serving as zero thickness reference measurements.

Submarines allow for long-range, basin-scale transects for determining the ice thickness profile. However, so far, submarine surveys have only been performed in conjunction with military cruises. This implies that transects are not designed with scientific priorities and in a systematic manner. As a consequence, measurements often have to be corrected for seasonal variability before they can be

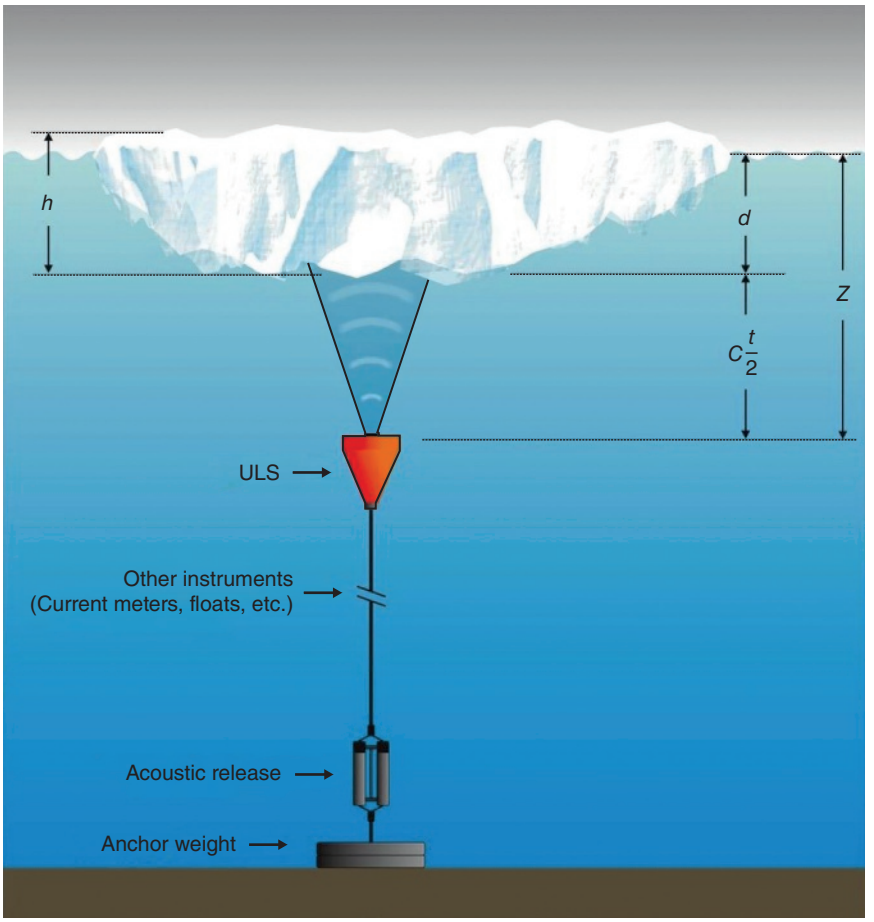


Figure 1.6 Schematic of a moored upward-looking sonar (ULS), with *d*: sea ice draft, *z*: instrument depth, *h*: sea ice thickness, *c*: sound velocity, and *t*: two-way travel time. *Source*: Behrendt et al. (2013), CC-BY 3.0 License/Earth System Science Data/CC-BY 3.0.

compared with each other (Rothrock et al., 2008). The Scientific Ice Expeditions program of the US Navy facilitates timely release and scientific analysis of submarine data. Meanwhile, autonomous underwater vehicles are being developed, and they may provide an alternative for the use of submarines in the future (Dowdeswell et al., 2008; Williams et al., 2015). They can also be used in Antarctica, where the operation of military, nuclear submarines is prohibited by the Antarctic Treaty.

ULSs mounted on oceanographic moorings provide long time series of ice thickness in a single location. These allow studying the temporal development of the ITD, e.g. in the course of the growing season (Melling & Riedel, 2004; Mahoney et al., 2015; Metzger et al., 2021). Transects can be achieved if several moorings are simultaneously operated across a certain region, such as in the Fram Strait (Hansen et al., 2013) or the Beaufort Sea (Krishfield et al., 2014). Combined with ice drift velocity data retrieved from satellite remote sensing or buoys, mooring data allow for the calculation of ice volume or freshwater fluxes.

While moored ULS can provide very valuable continuous data, the operation of the instruments at water depths of 50–150 m for

periods of one or more years is still a technological challenge. Similarly, the recovery of the instruments is often difficult, or instruments may be lost, e.g. as a result of commercial trawl fishing. Moorings cannot be deployed in shallow waters, where they might be destroyed by scouring from ridge keels or icebergs.

Airborne electromagnetic induction sounding

In contrast to high-frequency radar echo sounding, frequency-domain electromagnetic (EM) induction sounding uses low-frequency EM signals between 1 and 100 kHz and has become a widely applied method. The technique is sensitive to the distribution of electrical conductivity in the underground and is traditionally employed in mineral exploration or groundwater mapping on land. The transmitter coil of an EM instrument generates a "primary" EM dipole field, which penetrates almost unaffectedly through the resistive ice, whose electrical conductivity typically ranges between 0 and 50 mS m^{-1} (milli-Siemens per meter), depending on ice type and season (Haas et al., 1997). However, in the highly conductive seawater, with conductivities ranging between 2400 mS m^{-1} in the Western Arctic and 2700 mS m^{-1} in the Southern Ocean, eddy currents are induced. These, in turn, induce a "secondary" EM field, which propagates back through the ice and whose amplitude and phase are measured by a receiver coil, relative to the primary field. The amplitude of the secondary field decreases exponentially with increasing distance between the instrument and the ice–water interface, which coincides with the bottom of the ice (Figure 1.7). Relations between the secondary field amplitude and the distance to the ice–water interface can be derived empirically by means of coincident measurements over drill holes or open water (Haas et al., 1997, 2009, 2017) or by forward modeling (Anderson, 1979; Pfaffling et al., 2007; Haas et al., 2021). In addition, the EM response depends on the signal frequency and coil orientation and spacing. If the sensor is carried by an airborne platform, its height has to be

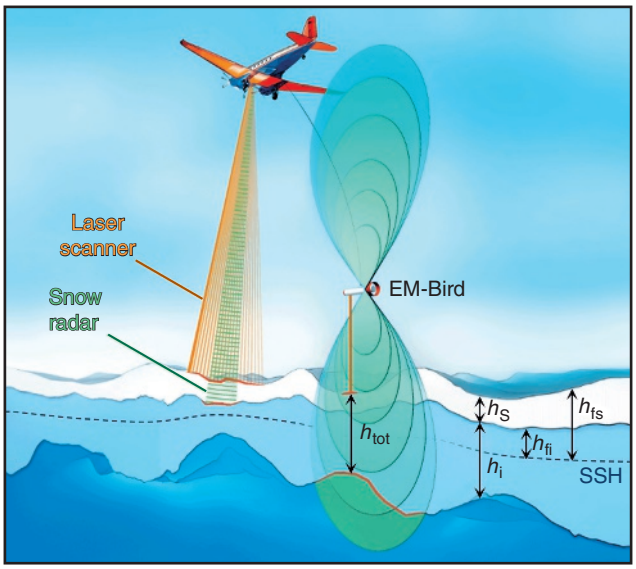


Figure 1.7 Illustration of airborne sea ice observations using an EM-Bird, a laser scanner, and a snow radar. The sea ice parameters relevant for these observations are total (ice + snow) thickness (h_{tot}), snow depth (h_s), sea ice thickness (h_i), sea ice freeboard (h_{fi}), and snow freeboard (h_{fs}). SSH stands for local sea surface height, depicted by the blue dashed line. *Source*: Jutila et al. (2022) / The Cryosphere / CC BY 4.0.

measured independently, typically using laser altimeters. Consequently, ice-plus-snow thickness can then be computed from the difference between the distance to the ice–water interface and the instrument height above the snow measured by the altimeter (Figure 1.7). To minimize disturbance from interference with conducting metallic parts of the aircraft and to facilitate operation close to the ice surface, the airborne sensors are typically operated as towed "Birds" (e.g. Kovacs & Holladay, 1990; Haas et al., 2009). The airborne platforms can be either helicopters or fixed-wing aircraft (e.g. Basler BT67 airplane; Haas et al., 2010). The ice thickness profile shown in Figure 1.3 was obtained with the surveying system similar to the one shown in Figure 1.7. Results from such surveys also provide validation for model results and satellite products. Comparisons with drill-hole data and theoretical considerations show that the accuracy of EM thickness measurements is better than ± 0.1 m over level ice (Haas et al., 1997; Pfaffling et al., 2007). However, due to the spatial extent of eddy currents induced in the water, the footprint of the method is quite large and can range between 3.7 and 10 times the distance between the EM instrument and the water surface, depending on the instrument configuration (Kovacs et al., 1995; Reid et al., 2006). Consequently, EM measurements underestimate the maximum thickness of narrow patches of deformed ice such as ridge keels by as much as 50% (Haas & Jochmann, 2003).

The EM induction sounding method continues to be used on the ground, where a sledge with an EM device is pulled by a person or snowmobile to measure ice thickness along the track (Haas et al., 2017; Itkin et al., 2023; Neudert et al., 2024).

Airborne laser altimetry

Like draft, sea ice freeboard is closely related to ice thickness via isostasy, and therefore, there are significant efforts to survey snow freeboard (Figure 1.5) using airborne laser altimetry, for example, as part of National Aeronautics and Space Administration's (NASA) Operation IceBridge mission, carried out from 2009 to 2019 (MacGregor et al., 2021). The principles of the method and conversion of freeboard to ice thickness are identical to satellite laser altimetry (Chapter 5). However, due to the lower flying altitudes of aircraft, the spatial resolution of individual measurements is significantly improved, and the use of scanning lasers provides two-dimensional freeboard and surface roughness information (Petty et al., 2016). Therefore, the full ITD can be resolved, and the data can be well analyzed for surface roughness and pressure ridge distributions (Tan et al., 2012; Castellani et al., 2014; Ricker et al., 2023).

In contrast to ULS measurements of sea ice draft, the uncertainty in altimetric ice thickness retrievals is much larger due to the small freeboard-to-thickness ratio. For a given freeboard error, the corresponding ice thickness uncertainty is approximately 10 times larger.

In addition, accurate knowledge of snow depth is required for reliable sea ice thickness retrievals. In contrast to satellite measurements, snow depth has successfully been measured from aircraft with FMCW radars (Panzer et al., 2013; Kwok et al., 2017; Jutila et al., 2022a; Fredensborg Hansen et al., 2024; see also Chapter 2), thus significantly improving ice thickness estimates.

Altimetric freeboard measurements also require accurate knowledge of the water level ("sea surface height") against which freeboard is referenced (Figure 1.5). Due to variable aircraft flying heights, unresolved geoid undulations, and dynamic sea surface topography, the height of the water level is generally poorly known and needs to be obtained from the altimetric measurements themselves. For high-resolution airborne measurements, this information can be obtained from the laser echo strength and from auxiliary photography of the location of open leads (Ricker et al., 2016). Overall, the uncertainty of laser altimetric mean ice thickness retrievals is estimated to be between 0.22 and 0.7 m (Kurtz et al., 2013). Note that due to the large uncertainties of altimetric ice thickness retrievals, many recent

laser altimetry studies focus on the observation of freeboard and snow thickness rather than ice thickness.

1.3.3 Global-scale observations

To assess global-scale changes of Earth's sea ice cover, spaceborne observations are crucial. While sea ice extent and concentration can be retrieved routinely from satellites since the 1980s (Chapter 5), sea ice thickness is more difficult to measure from space, since we need to infer accurate information in the third dimension. Satellite altimetry is the most common method to retrieve sea ice thickness from space. Radar (typically Ku-band, 12–18 GHz, 1.67–2.5 cm) or laser (typically in the green part of the visible spectrum) pulses are transmitted toward the surface and the travel time of the signal is recorded, allowing us to compute the distance between surface and satellite. By analyzing the characteristics of the reflected signal, surface heights from sea ice and from open water can be distinguished. The sea surface height, estimated by interpolation between open water tie points in leads (Figure 1.2), is then subtracted from the sea ice surface elevations to derive sea ice or snow freeboard depending on the used sensor (Figure 1.5; Ricker et al., 2016). While laser pulses are generally reflected at the snow surface, a radar signal can penetrate the snow to the snow–ice interface depending on the frequency (see Chapter 5 for more details). The derived freeboard is converted into sea ice thickness assuming hydrostatic equilibrium. This conversion requires information on sea ice density, which is challenging due to the lack of observations across the polar regions. Typically, bulk densities are estimated using parametrizations (e.g. Jutila et al., 2022b) or climatologies (Warren et al., 1999). Considering their large spatial and temporal variability, along with snow depth, ice densities are a major source of uncertainty in the freeboard-to-thickness conversion.

The European Space Agency (ESA) ERS1/2 satellite missions in the 1990s were the first carrying altimeters that have been used to derive sea ice thickness (Laxon et al., 2003). However, spatial resolution was relatively low, allowing only large-scale estimates, not resolving regions of deformed sea ice. With time, sensors became more advanced, and the ESA Satellite CryoSat-2 launched in 2010 for the first time allowed to routinely produce monthly maps of Arctic winter sea ice thickness (Tilling et al., 2018). Data fusion techniques (Ricker et al., 2017) and machine learning techniques (Paul et al., 2018) are used to further decrease uncertainties and address data gaps during the summer melt season (Landy et al., 2022).

Figure 1.8 shows mean Arctic and Antarctic winter sea ice thickness maps derived from CryoSat-2 using the methods described earlier. These datasets are used to investigate interannual large-scale changes in the ITD. However, it is still challenging to infer information on smaller scales (<100 m). The NASA ICESat-2 satellite launched in 2018 allows sampling of sea ice surface heights every 70 cm using a laser altimeter with a footprint of only 11 m, which makes it possible to identify individual pressure ridges from satellite altimetry for the first time (Duncan & Farrell, 2022).

Over thin ice, relative thickness uncertainties of altimeters are typically higher. Therefore, satellite radiometers, which can measure thin ice thickness quite accurately, are used to complement altimetry measurements to achieve a better representation of the ITD across all thickness classes (Ricker et al., 2017). A future goal is to enhance spatial resolution, reduce uncertainties (such as those caused by snow cover, see Chapter 5), and better understand and quantify how small-scale processes like ridging and sea ice dynamics affect changes of the global ITDs.

1.3.4 Bridging the scales

Sea ice thickness may vary significantly at small scales due to the cumulative effects of dynamic processes over time, creating patterns that resemble signal noise. This becomes clear when

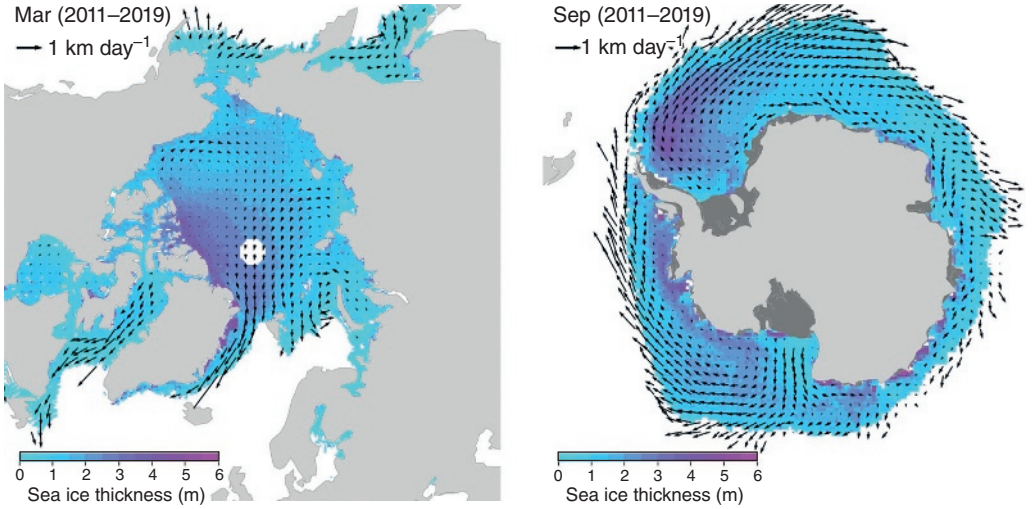


Figure 1.8 Sea ice thickness maps of the northern and southern hemispheres, derived from CryoSat-2, shown for March (Arctic) and September (Antarctic) averaged over the years 2011–2019. The sea ice thickness estimates come from the European Space Agency Climate Change Initiative Climate Data Record (Hendricks et al., 2024a, b). The arrows indicate the sea ice drift averaged over the same period. The drift data have been retrieved from the Ocean and Sea Ice Satellite Application Facility (OSI SAF) sea ice drift climate data record (OSI-455).

considering small sections of a few kilometers along the profile in Figure 1.3. Then, if we consider the entire profile over 65 km however, we find different ice thickness regimes, e.g. heavily ridged, thick sea ice (at km 40–55) and thin level ice of a refrozen lead (at ~60 km). When we zoom out even further, considering pan-Arctic scales (Figure 1.8), we see large patterns of thick and thin ice regimes. Those patterns are an aggregation of small-scale features as observed in Figure 1.3. Bridging these scales with observational methods is important to better understand how local sea ice dynamics affect large-scale patterns and to evaluate the realism of sea ice models as their spatial resolution increases.

However, seamless thickness observations across different scales are highly challenging due to limitations of the different methods (Figure 1.5). On-ground thickness observations can capture the ITD at kilometer-scale resolution, but they cannot be consistently maintained across the entire Arctic on a regular basis. On the other hand, airborne – and even more so, satellite – measurements are limited in accuracy and spatial resolution due to their increasing distance from the surface, requiring the use of different sensors and methods. Eventually, achieving sufficient coverage across the poles involves a trade-off between accuracy and scope. Thus, studies linking multiple measurements across different scales are needed (e.g. between ULS/ALS and satellite altimeters such as CryoSat-2 or ICESat-2). With upcoming advancements in measurement techniques (see Section 1.6), we expect to gain a better understanding of how small-scale dynamic processes in the sea ice cover are connected to large-scale patterns of sea ice thickness.

1.4 Global sea ice thickness distributions

In the previous sections, we have described the physical processes of dynamics and thermodynamics forming ridges and leads and thus forming heterogeneous sea ice thickness on meter scales. Satellites and models are

usually not able to resolve such small features. However, due to differences in ocean currents, atmospheric patterns, and shorelines that form barriers, small-scale thickness variability translates into large patterns of different sea ice thickness regimes. Mean wintertime sea ice thickness fields and ice drift between 2011 and 2019 are shown in Figure 1.8. The sea ice thickness estimates are derived from CryoSat-2 altimeter measurements and are based on an algorithm that has been developed within the ESA Climate Change Initiative to generate long data records of sea ice variables, including sea ice thickness (Hendricks et al., 2024a, b). The sea ice drift is derived from passive microwave satellite sensors over the same period (Chapter 5; Lavergne & Down, 2023). The large regional differences within each hemisphere shown in Figure 1.8 are primarily a result of ice motion and deformation. The mean thickness of an ice field is heavily influenced by the presence of pressure ridges. Consequently, the number and thickness of these ridges play a more significant role in determining regional mean ice thickness than the thermodynamic thickness of level ice. Therefore, on a regional scale, the average ITD is determined by the prevailing atmospheric circulation regimes, which are responsible for mean ice motion and the dominant drift directions. Where the ice drifts against, or shears along a coastline, it leads to substantial ice pressure and significant deformation. As a result, the mean thickness in regions with mean drift convergence is larger than in regions with mean divergence.

The arrows in Figure 1.8 illustrate the dominant drift patterns that emerge due to the prevailing atmospheric circulation in both hemispheres. In the Arctic, two main drift systems exist. The Beaufort Gyre is an anticyclonic gyre in the Canada Basin. It is caused by quasi-permanent high atmospheric pressure over the Beaufort Sea. The Beaufort Gyre can transport ice floes for several years before they are exported into the Transpolar Drift. This is the other prominent drift system, which transports ice from the source regions on the Siberian Shelves within about 1–3 years across the North Pole into Fram Strait and the East Greenland Current, where it finally melts. The Transpolar Drift is mainly driven by low-pressure systems passing from the North Atlantic into the Barents and Kara Seas. On average, these drift patterns push the ice against the coasts of northern Canada and Greenland. Consequently, because of strong convergence and deformation, the thickest ice is found in these regions as shown in Figure 1.8. Here, the mean maximum thicknesses often exceed 4 m, mainly resulting from the large spatial density of thick ridges that have been formed over several seasons. The youngest and thinnest ice is found along the Siberian Shelf, where prominent polynyas occur and from where newly grown ice is continuously exported into the Transpolar Drift (Krumpen et al., 2019). In winter, sea ice also extends further to the south and a discussion of sea ice thickness in those Arctic Marginal Seas is detailed in Chapter 22.

The spatial ITDs shown in Figure 1.8 are in good qualitative agreement with airborne observations (Ricker et al., 2017; Tilling et al., 2018) and maps of modelled ice thickness (Boutin et al., 2023).

Considering the Southern Hemisphere, Figure 1.8 shows that thicker ice in Antarctica is found close to the continent, in accordance with the greatest proximity to the pole, and in the vicinity of the coast where it is sporadically compressed. The most prominent feature is the thickest ice in the western Weddell Sea. On the one hand, this is one of a few regions in the Southern Hemisphere where perennial ice, i.e. MYI, exists. On the other hand, it is a region where ice drift is directed toward the coast, and subsequently much deformation occurs. The so-called Weddell Gyre is caused by low average sea level pressure over the central Weddell Sea. It should be noted that both the Beaufort Gyre and the Weddell Gyre rotate clockwise. However, due to the Coriolis force, this results in ice convergence within the gyre center on the Northern

Hemisphere, whereas clockwise circulation results in net divergence inside the gyre in the south. The exceptionally thick sea ice in the western Weddell Sea is, therefore, caused by ice motion away from the divergent gyre center, with the Antarctic Peninsula being an obstacle to the drifting ice.

In past decades, the Arctic lost much of its older thick ice (Sumata et al., 2023), while until recently, Antarctic sea ice showed even a slight increase in extent, with significant regional variability (Turner et al., 2015). Therefore, while decades ago, Arctic sea ice was considered generally thicker than its counterpart around Antarctica, this difference has become more subtle in recent years with the Arctic more and more dominated by FYI. Contrasts between both hemispheres are due to at least five main differences in the thermodynamic and dynamic boundary conditions of ice growth in the Arctic and Southern Ocean (see also Chapter 6):

1. Ocean heat flux:
   A fundamental difference between the Arctic and Southern Oceans is the much stronger stratification of the Arctic Ocean that prevents any upward mixing of heat from the deeper ocean. The strong stratification is due to a fresh mixed layer in the Arctic Ocean disconnected from the warmer, more saline deeper ocean. This layer is fed by the inflow of fresh water from large rivers, mainly from the Siberian continent. The Arctic Ocean receives approximately 10% of the world river run-off. The fresh mixed layer is very stable and prohibits any significant heat fluxes from the much warmer Atlantic water underneath. A typical value for the ocean heat flux in the Arctic Ocean is in the range of 2–8 W m^{-2}. The *Atlantic layer* at a depth of 200–300 m is 1–2 °C warm. This heat would be sufficient to melt all ice during summer (Barry et al., 1993). In the Southern Ocean, no rivers enter the seas and icebergs melt further to the north. Therefore, the mixed layer is much saltier and not well stratified. Mean vertical ocean heat fluxes to the sea ice amount to between 8 and more than 20 W m^{-2} with large regional variability (Ackley et al., 2015). However, in the past decades, we have observed a growing impact of Atlantic water flowing into the Arctic Ocean in connection with the disruption of stratification. This causes the warm Atlantic water to mix with the fresh water at the surface (Polyakov et al., 2017, 2023), reducing the sea ice growth during the freeze-up, especially in the European sector of the Arctic (Belter et al., 2021; Ricker et al., 2021).
2. Snow depth:
   With a thermal conductivity between 0.11 and 0.35 W m^{-1} K^{-1} (Chapter 2; Massom et al., 2001), snow is a strong thermal insulator. Therefore, ice with a thick snow cover grows slower than if the snow were thin. The Arctic Ocean is surrounded by large landmasses, and during winter, the limited availability of moisture sources leads to relatively low precipitation. As a result, average snow depths on perennial ice in spring are only about 0.3 m (Warren et al., 1999; Webster et al., 2018). In contrast, Antarctic sea ice is usually covered by thick snow. On perennial ice in the Pacific sector or in the western Weddell Sea, the mean snow thickness can be larger than 0.5 m (Massom et al., 2001; Kwok & Maksym, 2014; Arndt et al., 2021). This is because the sea ice areas are surrounded by oceans providing a permanent moisture source. As a consequence of the thick, insulating snow and the high ocean heat fluxes, Antarctic ice may melt at its underside even during winter, because the temperature gradients through the ice are only small (Lytle & Ackley, 1996; Maksym et al., 2012). On the other hand, the load of thick snow on thin sea ice can lead to flooding of the ice surface with sea water. This can lead to the formation of so-called *snow ice* – refrozen slush, which, in turn,

can contribute significantly to the sea ice mass balance (Chapter 2; Massom et al., 2001). Along with the decreasing ice thickness in the Arctic during the past decades, flooding of the snow over thinner ice could become more common also in the Northern Hemisphere (Rösel et al., 2018).

3. Ice age:
   Although the area of old ice in the Arctic has decreased strongly in the past decades (Moon et al., 2023), a significant amount of Arctic sea ice still drifts for at least two years until it melts in summer or until it leaves the Basin mostly through Fram Strait, where it melts further south. The older the sea ice becomes, the more deformation events can thicken it by compressing it into pressure ridges (Krumpen et al., 2025). This dynamic thickening is accompanied by passing through several winters where the ice can also thicken by thermodynamic growth until it reaches an equilibrium thickness. In contrast, most Antarctic ice melts during summer. Thus, it rarely becomes older than one year, and only a few regions with perennial ice exist in the western Weddell Sea and southern Bellingshausen, Amundsen, and Ross Seas.
4. Drift patterns:
   The Arctic Ocean is surrounded by continents, and thus sea ice motion is confined by coasts where the ice converges and thickens by deformation, particularly north of Canada and Greenland. In contrast, ice drift around Antarctica is mostly divergent with a net northerly drift component toward the surrounding open oceans. This divergence also causes the opening of polynyas and leads, where new thin ice forms, which alters the thickness distribution.
5. Geographic Disparity:
   Most of the sea ice in the Arctic is at latitudes north of 70 °N, whereas in the Southern Hemisphere, most sea ice extends into much lower latitudes, as far north as 55 °S. Thus, air temperatures, total incoming solar radiation, and the length of the summer season are generally lower in the Arctic than in the Southern Ocean. However, the Antarctic ice sheet is a giant cold reservoir, and the sea ice region is well isolated from lower latitudes by the atmospheric and oceanic flow regimes of the Antarctic Circumpolar Current. Therefore, warm and moist air advection are not as impactful as they are for the Arctic, where land masses and ocean currents support their transport to high latitudes. This leads to the striking difference that strong surface melting occurs in summer even at the North Pole while melt ponds are rarely observed on Antarctic sea ice at much lower latitudes.

The resulting global-scale ice thickness is conditioned upon the magnitude and interplay of these various aspects. In contrast to the Arctic, regional ITDs in the Antarctic are less well known, because only a few systematic measurements have been performed. However, thickness maps derived from visual observations (Worby et al., 2008), airborne measurements (Kwok & Maksym, 2014), as well as satellite missions like CryoSat-2 or ICESat-2 (Kacimi & Kwok, 2020; Bocquet et al., 2024) show similar patterns as those shown in Figure 1.8. It should be noted that the drift systems and thickness distributions shown in Figure 1.8 represent long-term average conditions. There is large seasonal, interannual, and decadal variability superimposed on these mean patterns.

1.5 Dynamic and thermodynamic thickness changes and long-term trends

1.5.1 Dynamic and thermodynamic thickness change

Sea ice thickness is at the center of the ongoing changes in the Arctic because it regulates key processes of the Arctic climate system. Recent studies have analyzed and quantified the role of thermodynamics and dynamics in changing sea

ice thickness on pan-Arctic (e.g. Ricker et al., 2021; Anheuser et al., 2022) and regional scales (e.g. Koo et al., 2021; Albedyll et al., 2022). Ricker et al. (2021) analyzed ice advection, deformation, and thermodynamic growth in different regions of the Arctic Ocean combining long-term thickness and drift observations from satellites and model simulations (Figure 1.9). Overall, thermodynamic growth dominates the volume change on those large scales, while dynamic volume change differs significantly between regions. Figure 1.9 also illustrates the

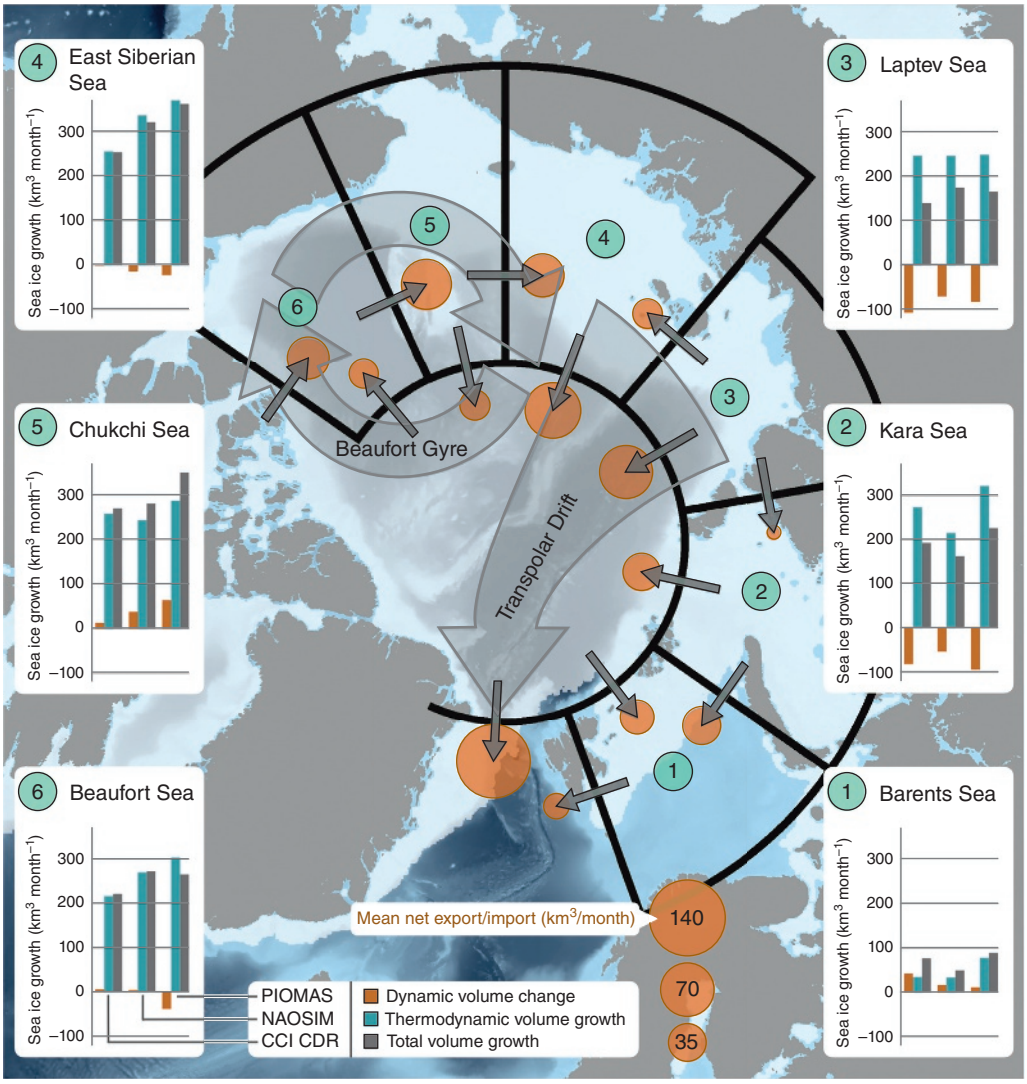


Figure 1.9 Selected Arctic regions and corresponding net winter (November–March) sea ice export/import through meridional and zonal boundaries from 2002 to 2019 using satellite-derived sea ice volume fluxes (orange slices). Bar charts illustrate mean winter dynamic ice volume growth, mean winter thermodynamic growth, and mean winter total volume growth from 2002 to 2019 from the North Atlantic/Arctic Ocean-Sea Ice Model (NAOSIM), from the Pan-Arctic Ice Ocean Modeling and Assimilation System (PIOMAS), and from the European Space Agency Climate Change Initiative Climate Data Record (CCI CDR). Negative values indicate net export or melt of sea ice. *Source*: Ricker et al. (2021)/American Meteorological Society [AMS]/ CC BY 4.0.

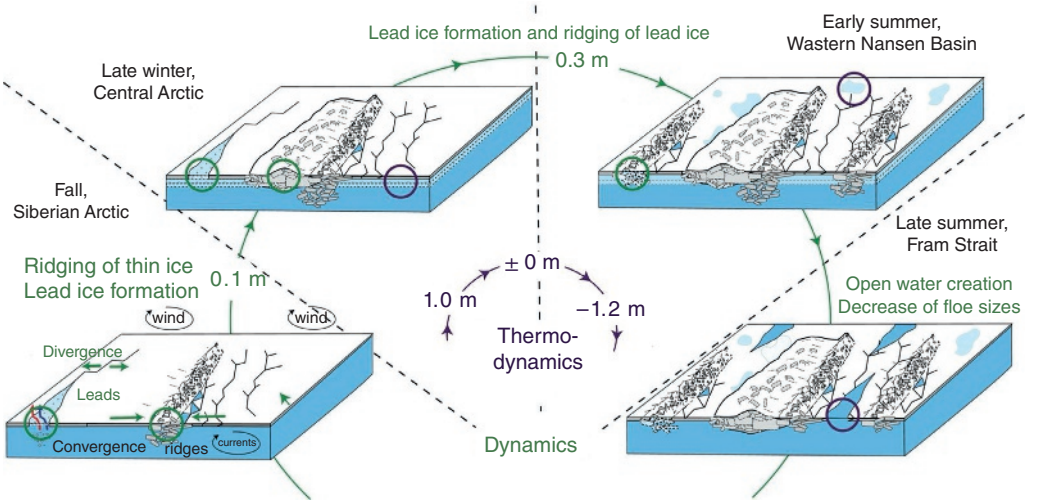


Figure 1.10 Seasonal/spatial cycle of sea ice dynamics and thermodynamics along the drift trajectory of the MOSAiC field campaign in 2019/2020 in the Transpolar Drift. *Source*: Albedyll et al. (2022), CC-BY 4.0 License/The Regents of the University of California/CC BY 4.0.

mean export of sea ice in the Laptev and Kara Seas, highlighting these regions as key areas of sea ice production, where new ice is continuously formed thermodynamically.

On local to regional scales, convergence can double the thermodynamic sea ice thickness. Thus, convergence plays a key role for the sea ice mass balance in geographic regions with predominantly convergent ice regimes for creating and maintaining a thick and stable ice cover (Kwok & Cunningham, 2016; Itkin et al., 2018; Albedyll et al., 2021; Koo et al., 2021). The local increase in thickness has consequences not only for the regional sea ice extent and summer melt but also for the local ecosystem as it provides a stable habitat and platform for resting and hunting for marine mammals (Post et al., 2013; Schweiger et al., 2021). Divergence reduces the mean thickness by adding open water but increases the overall sea ice volume by enhancing new ice formation in winter. Depending on the dynamic ice regime, divergence-induced new ice formation contributes between 7% and 40% to the Arctic sea ice mass balance (Koerner, 1973; Kwok, 2006; Itkin et al., 2018; Albedyll et al., 2022), although leads are typically short-lived (days) and cover an area of a few percent (Wadhams, 2000; Hutter et al., 2019; Reiser et al., 2020; von Albedyll et al., 2024). As an example, Figure 1.10 shows how sea ice deformation impacted the regional sea ice mass balance along the drift trajectory of the MOSAiC field campaign in 2019/2020 in the Transpolar Drift (Albedyll et al., 2022).

Recently, the contribution of dynamics and thermodynamics to the sea ice mass balance was also analyzed in sea ice and climate models (Keen et al., 2021; Smith et al., 2022; Boutin et al., 2023).

1.5.2 Long-term trends

Observations from satellites (Kwok, 2018; Kacimi & Kwok, 2022; Landy et al., 2022; Bocquet et al., 2024), upward-looking sonars on submarines (e.g. Rothrock et al., 1999, 2008), or anchored moorings (e.g. Sumata et al., 2023), as well as airborne and *in situ* campaigns (e.g. Haas et al., 2008; Belter et al., 2021), have reported on a decline of annual mean sea ice thickness at a rate of about 10% per decade between 1958 and 2018 (Figure 1.11; Chapter 7; Meier et al., 2014; Lindsay & Schweiger, 2015; Kwok, 2018;

Stroeve & Notz, 2018). Most of this change happened before 2011; thereafter, the mean thickness trends were negligible (Kwok, 2018; Kacimi & Kwok, 2024) despite rising air temperatures. However, there are regional and seasonal differences in the thickness decline. For example, the strongest ice thickness change occurred at the North Pole where the ice has also continued to thin over the past decade as a result of replacement of older ice with FYI (Kwok, 2018; Krumpen et al., 2025).

Most of the Arctic sea ice thinning and volume loss is associated with the decrease in sea ice age (Tschudi et al., 2016; Kwok, 2018; Perovich et al., 2020; Sumata et al., 2023). The substantial loss of MYI is caused by decreasing summer ice extent and, therefore, larger regions of FYI formation and higher ice drift speeds that reduce the residence time of ice in the Arctic Ocean (Stroeve & Notz, 2018; Sumata et al., 2023; Krumpen et al., 2025). Rising air temperatures due to atmospheric greenhouse gas concentrations caused by anthropogenic emissions can explain most of the enhanced sea ice melting (e.g. Niederdrenk & Notz, 2018), but there is

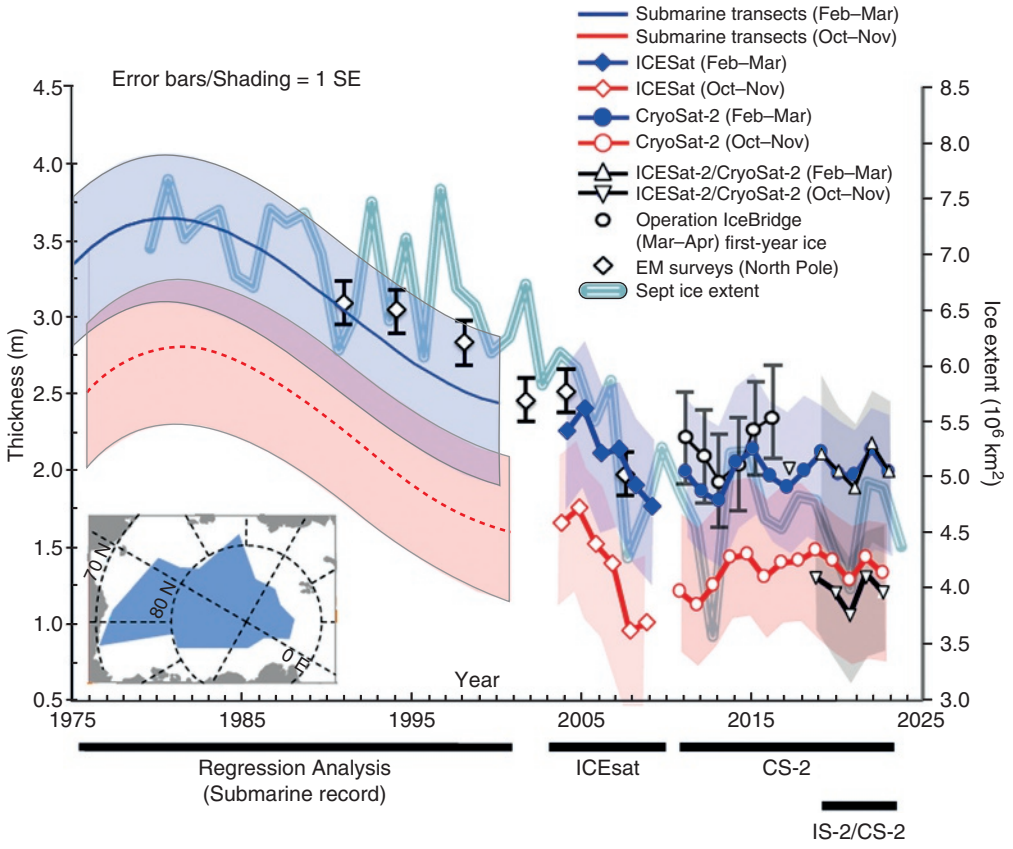


Figure 1.11 Arctic sea ice thickness changes (means) for autumn (red/dotted red) and winter (blue/dotted blue). Shadings (blue and red) show 1 standard error (SE) ranges from the regression analysis of submarine ice thickness and expected uncertainties in satellite ice thickness estimates. Data release area of submarine data ice thickness data is shown in the inset. Satellite ice thickness estimates are for the Arctic south of 88 °N. Thickness estimates from more localized airborne/ground electromagnetic (EM) surveys near the North Pole (diamonds) and from Operation IceBridge (circles) are shown within the context of the larger scale changes in the submarine and satellite records. *Source*: Kacimi & Kwok (2024), CC-BY 4.0 License/ MDPI/CC BY 4.0.

also growing evidence for enhanced ocean heat flux to the ice due to a destabilized halocline ("Atlantification"; see Chapter 8) that mitigates winter freezing and accelerates summer melt (Ricker et al., 2021; Polyakov et al., 2023). The reduced residence time leads to a thinner, more uniform ice regime with less ridges as the ice has less time to experience deformation events (Figure 1.12).

Recent observational and modeling studies also explored the potential of stabilizing or negative feedback loops in the "New Arctic." Strongly linked to ice thickness is the ice growth feedback that describes that thin ice or ice forming from open water, e.g. on the ice-free Siberian shelves in autumn, grows quicker than thicker ice during the winter, compensating partly for the ice thinning (Ricker et al., 2021). However, the efficiency of this feedback may have already reached its maximum (Stroeve et al., 2018; Cornish et al., 2022). While the freezing efficiency increases due to the ice growth feedback, the number of freezing days decreases, because the ocean accumulates more heat during a longer ice-free season that needs to be extracted before freeze-up. Increased dynamic thickening and enhanced new ice formation due to more ridging and lead formation as a consequence of a reduced ice strength seem plausible; however, observational studies focusing on Arctic lead fractions and LKFs could not (yet) confirm such a temporal trend of increased dynamic thickening (Wang et al., 2016; Willmes & Heinemann, 2016; Hutter & Losch, 2020; Krumpen et al., 2025). Further negative feedback is associated with the increase in outgoing longwave radiation during winter and less snow accumulation on sea ice during winter resulting in quicker ice growth (Chapter 10; Notz, 2009; Tietsche et al., 2011).

1.5.3 Consequences of thinner ice

A thinner ice cover has multiple implications for the Arctic climate and ecosystem that include, but are not limited to, a general reduction in sea ice extent, enhanced seasonality in ice thickness (Massonnet et al., 2018), greater interannual variability in ice extent (e.g. Notz, 2009; Mioduszewski et al., 2019), increased under-ice light availability

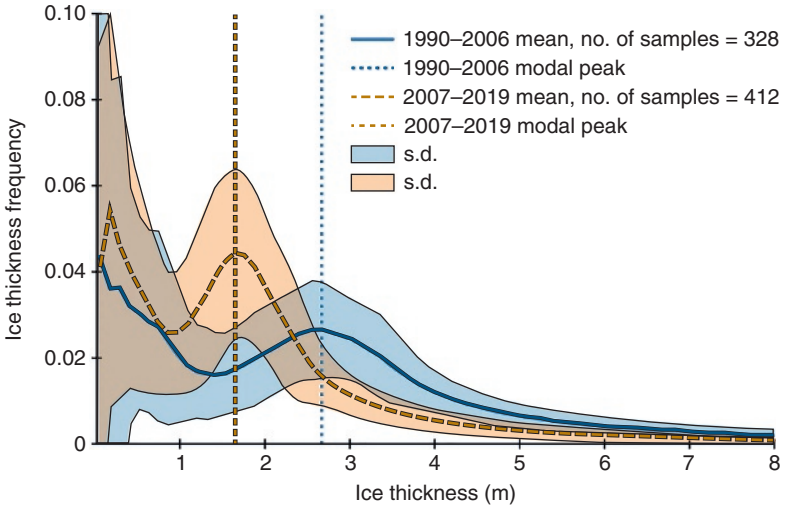


Figure 1.12 Mean sea ice thickness distribution in the Fram Strait before and after 2007, based on upward-looking sonar measurements in the Fram Strait. *Source*: Sumata et al. (2023), CC-BY 4.0 License/ Springer Nature/CC-BY 4.0.

(e.g. Castellani et al., 2021), reduced freshwater export to sub-Arctic seas (e.g. Wang et al., 2021), reduced resting, reproduction, and hunting opportunities for marine mammals (e.g. Post et al., 2013), changes in economic exploration (e.g. Gautier et al., 2009; Khon et al., 2009), and an interrupted sediment transport (e.g. Krumpen et al., 2019). With the transition from predominantly MYI to FYI in large areas of the Arctic, ocean and air drag also reduces (Petty et al., 2017; Krumpen et al., 2025), with an expected impact on the momentum exchange.

1.5.4 Antarctic sea ice thickness change

Long-term observations of Antarctic sea ice thickness using radar altimetry are sparse as the retrieval of sea ice thickness is complicated due to the thick and complex snowpack (see "snow ice formation" and Chapter 2). Unlike the Arctic, where sea ice has shown a clear and consistent decline, the ice around Antarctica changed relatively little over most of the same period. Thickness estimates based on CryoSat-2 measurements show small but competing regional thickness changes between 2010 and 2021 (Fons et al., 2023; Bocquet et al., 2024). However, since 2017, Antarctic sea ice experienced sudden drops in extent (Purich & Doddridge, 2023). The cause for this recent decline and its impact on the ITD are currently under investigation. Chapters 6 and 10 discuss the recent trends in more detail.

1.6 Recent advancements and future directions

1.6.1 Sea ice thickness from satellites during summer

As described in Section 1.3.3 and Chapter 5, global-scale sea ice thickness is primarily derived from satellite altimetry, for which the discrimination between open water in leads and ice floes is essential. However, during summer, melt ponds complicate the separation as their radar signature is very similar to those of leads, but their water level may not be at sea level. Therefore, the estimation of freeboard is difficult. To overcome this challenge, Landy et al. (2022) introduce a novel approach utilizing deep learning techniques and numerical simulations of the CryoSat-2 radar altimeter response to better identify returns from leads and to finally derive a year-round pan-Arctic sea ice thickness dataset. The obtained data provide valuable insights into the changing Arctic climate and open up new possibilities for enhancing sea ice forecasting in summer, with implications for the safety of maritime activities and understanding climate feedback on different timescales.

1.6.2 Ice thickness distributions from the next-generation satellite altimeters

Present and future satellite altimeters with advancements in sensor development allow for higher spatial resolution and improved precision in elevation retrievals. The NASA ICESat-2 satellite is equipped with a photon-counting laser altimeter, sensing the surface with six parallel beams that are arranged in three pairs. Each beam has a nominal footprint diameter of around 11 m (Magruder et al., 2020). Together with the high pulse repetition rate, this allows for unprecedented measurements of sea ice surface topography, and eventually retrievals of freeboard and thickness. In fact, in several studies (Farrell et al., 2020; Duncan & Farrell, 2022; Ricker et al., 2023), it has been demonstrated that it is possible to detect pressure ridges and even estimate their heights (Figure 1.13). With the capability to capture individual pressure ridges, the tail of the ITD – the thick ice fraction (Figure 1.3) – will be better represented in thickness retrievals from next-generation satellite altimeters.

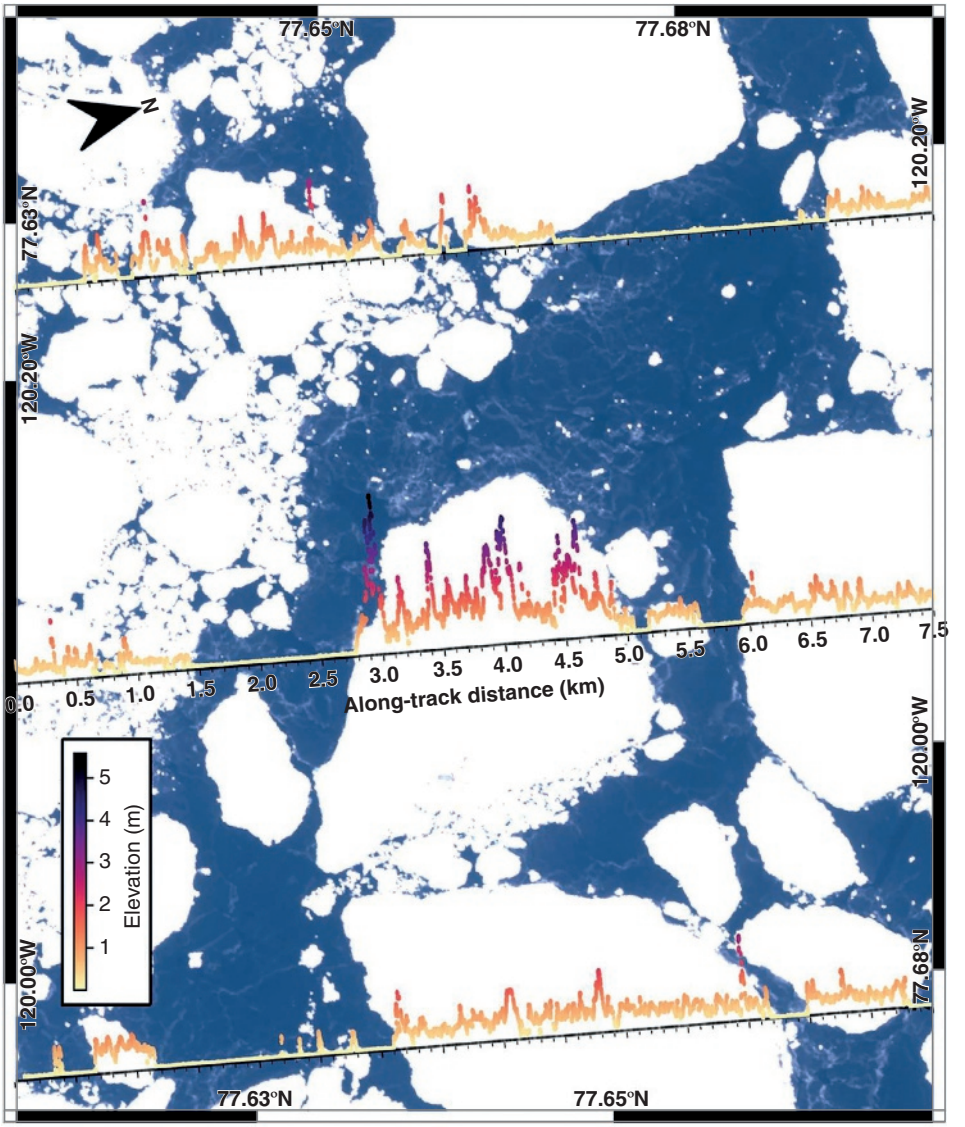


Figure 1.13 Sea ice elevation (7.5-km-long) profiles from 3 September 2019 in the Western Arctic, derived from three ICESat-2 beams. The background shows a coincident Sentinel-2 image. *Source*: Farrell et al. (2020)/American Geophysical Union/CC BY 4.0.

While ICESat-2 is already operational, the upcoming dual-frequency Ku/Ka-band CRISTAL mission will allow for simultaneous retrieval of snow depth and sea ice thickness, achieving a resolution of less than 100 m along track (Kern et al., 2020). This advancement is expected to substantially reduce sea ice thickness uncertainties caused by the snow layer and greatly improve the ability to detect small-scale variations in the ITD.

1.6.3 Monitoring platelet ice with EM induction sounding

Along the coast of Antarctica, the melting of ice shelves generates supercooled "Ice Shelf

Water" (ISW) that flows under adjacent landfast sea ice that fringes the ice shelf edges (see Chapter 6). The supercooled water leads to the formation of large ice crystals under the consolidated fast ice, so-called platelet ice (Hoppmann et al., 2020). Platelet ice may either be incorporated by the growing, consolidated ice from above or may form a porous sub-ice platelet layer (SIPL; Langhorne et al., 2015). SIPLs strongly contribute to the growth and thickening of landfast ice, form a unique ecological habitat, and are important indicators for basal melt processes under ice shelves (Hoppmann et al., 2020). Due to their buoyancy, they can increase sea ice freeboard, which leads to significant overestimation of sea ice thickness retrievals from altimetry (Price et al., 2014). However, since platelet ice is located below the ice, it is difficult to detect from above.

Recently, EM induction sounding has been used to detect SIPLs and to measure their thickness. This takes advantage of the fact that the SIPL is porous, and seawater filled, and therefore, its electrical conductivity is in between that of seawater (typically 2700 mS m^{-1} in the Southern Ocean) and consolidated ice (typically few tens of mS m^{-1}). Various studies have applied ground-based, single or multifrequency EM sensors to map the thickness and conductivity of the SIPL or to study its temporal development (Hunkeler et al., 2016; Brett et al., 2024; Neudert et al., 2024). Inversions were also developed for airborne EM surveys of the presence and thickness of the SIPL, offering the opportunity to map the SIPL all along the ice shelf fronts of Antarctica and to detect and study regions of intense ISW outflow (Haas et al., 2021; Langhorne et al., 2023).

Figure 1.14 shows a time series of EM measurements on fast ice in McMurdo Sound, Antarctica. The EM platelet ice thickness time series demonstrates the capability of this method to provide high-resolution temporal monitoring compared to occasional drill-hole measurements.

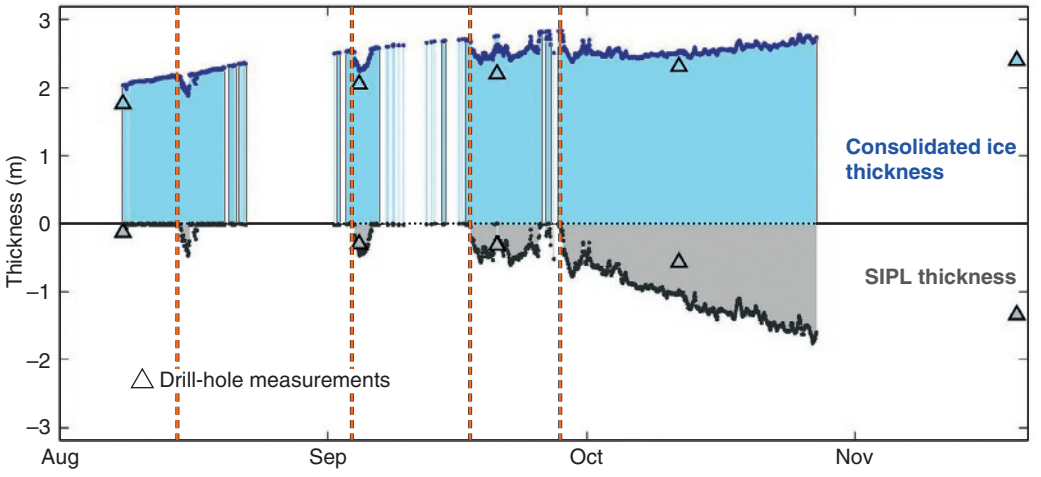


Figure 1.14 Time series of consolidated ice and sub-ice platelet layer thickness derived from electromagnetic thickness sounding between 8 August and 27 October 2018, on fast ice in McMurdo Sound, western Ross Sea. Drill-hole measurements are highlighted as triangles. Vertical dashed red lines indicate the onset of platelet ice growth events. SIPL, sub-ice platelet layer. *Source*: Brett et al. (2024), CC-BY 4.0 License/The Cryosphere/CC BY 4.0.

Future developments in EM sounding will focus on the better usage and inversion of multifrequency data and their application for the joint retrieval of ice thickness and other sea ice properties like porosity and presence and thickness of slush at the snow–ice interface.

References

Ackley, S.F., Xie, H. & Tichenor, E.A. (2015) Ocean heat flux under Antarctic sea ice in the Bellingshausen and Amundsen Seas: two case studies. *Annals of Glaciology*, **56**, 200–210, https://doi.org/10.3189/2015AoG69A890.

Amundrud, T.L., Melling, H. & Ingram, R.G. (2004) Geometrical constraints on the evolution of ridged sea ice. *Journal of Geophysical Research*, **109**, C06005, https://doi.org/10.1029/2003jc002251.

Amundrud, T.L., Melling, H., Ingram, R.G. & Allen, S.E. (2006) The effect of structural porosity on the ablation of sea ice ridges. *Journal of Geophysical Research: Oceans*, **111**, https://doi.org/10.1029/2005JC002895.

Anderson, W.L. (1979) Numerical integration of related Hankel transforms of orders 0 and 1 by adaptive digital filtering. *Geophysics*, **44**, 1287–1305, https://doi.org/10.1190/1.1441007.

Anheuser, J., Liu, Y. & Key, J.R. (2022) A climatology of thermodynamic vs. dynamic Arctic wintertime sea ice thickness effects during the CryoSat-2 era. *The Cryopshere Discussion*, https://doi.org/10.5194/tc-2022-218.

Arndt, S., Haas, C., Meyer, H., Peeken, I. & Krumpen, T. (2021) Recent observations of superimposed ice and snow ice on sea ice in the northwestern Weddell Sea. *The Cryosphere*, **15**, 4165–4178, https://doi.org/10.5194/tc-15-4165-2021.

Arntsen, A.E., Song, A.J., Perovich, D.K. & Richter-Menge, J.A. (2015) Observations of the summer breakup of an Arctic sea ice cover. *Geophysical Research Letters*, **42**, 8057–8063, https://doi.org/10.1002/2015gl065224.

Barry, R.G., Serreze, M.C., Maslanik, J.A. & Preller, R.H. (1993) The Arctic sea ice-climate system: observations and modeling. *Reviews of Geophysics*, **31**, 397–422, https://doi.org/10.1029/93RG01998.

Behrendt, A., Dierking, W., Fahrbach, E. & Witte, H. (2013) Sea ice draft in the Weddell Sea, measured by upward looking sonars. *Earth System Science Data*, **5**, 209–226, https://doi.org/10.5194/essd-5-209-2013.

Belter, H.J., Krumpen, T., von Albedyll, L., Alekseeva, T.A., Birnbaum, G., Frolov, S.V., et al. (2021) Interannual variability in Transpolar Drift summer sea ice thickness and potential impact of Atlantification. *The Cryosphere*, **15**, 2575–2591, https://doi.org/10.5194/tc-15-2575-2021.

Bocquet, M., Fleury, S., Rémy, F. & Piras, F. (2024) Arctic and Antarctic sea ice thickness and volume changes from observations between 1994 and 2023. *Journal of Geophysical Research: Oceans*, **129**, e2023JC020848, https://doi.org/10.1029/2023JC020848.

Bourke, R.H. & Garrett, R.P. (1987) Sea ice thickness distribution in the Arctic Ocean. *Cold Regions Science and Technology*, **13**, 259–280, https://doi.org/10.1016/0165-232X(87)90007-3.

Boutin, G., Ólason, E., Rampal, P., Regan, H., Lique, C., Talandier, C., et al. (2023) Arctic sea ice mass balance in a new coupled ice–ocean model using a brittle rheology framework. *The Cryosphere*, **17**, 617–638, https://doi.org/10.5194/tc-17-617-2023.

Brett, G.M., Leonard, G.H., Rack, W., Haas, C., Langhorne, P.J., Robinson, N.J. et al. (2024) Seasonal and diurnal variability of sub-ice platelet layer thickness in McMurdo Sound from electromagnetic induction sounding. *The Cryosphere*, **18**, 3049–3066, https://doi.org/10.5194/tc-18-3049-2024.

Castellani, G., Lüpkes, C., Hendricks, S. & Gerdes, R. (2014) Variability of Arctic sea-ice topography and its impact on the atmospheric surface drag. *Journal of Geophysical Research: Oceans*, **119**, 6743–6762, https://doi.org/10.1002/2013jc009712.

Castellani, G., Veyssière, G., Karcher, M., Stroeve, J., Banas, S.N., Bouman, A.H., et al. (2021) Shine a light: under-ice light and its ecological implications in a changing Arctic Ocean. *Ambio*, **51**, 307–317, https://doi.org/10.1007/s13280-021-01662-3.

Cornish, S.B., Johnson, H.L., Mallett, R.D.C., Dörr, J., Kostov, Y. & Richards, A.E. (2022) Rise and fall of sea ice production in the Arctic Ocean's ice factories. *Nature Communications*, **13**, https://doi.org/10.1038/s41467-022-34785-6.

Dowdeswell, J.A., Evans, J., Mugford, R., Griffiths, G., McPhail, S., Millard, N., et al. (2008) Autonomous underwater vehicles (AUVs) and investigations of the ice–ocean interface in Antarctic and Arctic waters. *Journal of Glaciology*, **54**, 661–672.

Duncan, K. & Farrell, S.L. (2022) Determining variability in Arctic Sea Ice pressure ridge topography with ICESat-2. *Geophysical Research Letters*, **49**, e2022GL100272, https://doi.org/10.1029/2022gl100272.

Eicken, H., Lensu, M., Leppäranta, M., Tucker III, W.B., Gow, A.J. & Salmela, O. (1995) Thickness, structure, and properties of level summer multiyear ice in the Eurasian sector of the Arctic Ocean. *Journal of Geophysical Research: Oceans*, **100**, 22697–22710, https://doi.org/10.1029/95JC02188.

Farrell, S.L., Duncan, K., Buckley, E.M., Richter-Menge, J. & Li, R. (2020) Mapping sea ice surface topography in high fidelity with ICESat-2. *Geophysical Research Letters*, **47**, e2020GL090708, https://doi.org/10.1029/2020gl090708.

Flato, G.M. & Hibler, W.D. (1995) Ridging and strength in modeling the thickness distribution of Arctic sea ice. *Journal of Geophysical Research*, **100**, 18611, https://doi.org/10.1029/95jc02091.

Fons, S., Kurtz, N. & Bagnardi, M. (2023) A decade-plus of Antarctic sea ice thickness and volume estimates from CryoSat-2 using a physical model and waveform fitting. *The Cryosphere*, **17**, 2487–2508, https://doi.org/10.5194/tc-17-2487-2023.

Fredensborg Hansen, R.M., Skourup, H., Rinne, E., Jutila, A., Lawrence, I.R., Shepherd, A., et al. (2024) Exploring microwave penetration into snow on Antarctic summer sea ice along CryoSat-2 and ICESat-2 (CRYO2ICE) orbit from multi-frequency air- and spaceborne altimetry. *EGUsphere*, **2024**, 1–53, https://doi.org/10.5194/egusphere-2024-2854.

Galley, R.J., Trachtenberg, M., Langlois, A., Barber, D.G. & Shafai, L. (2009) Observations of geophysical and dielectric properties and ground penetrating radar signatures for discrimination of snow, sea ice and freshwater ice thickness. *Cold Regions Science and Technology*, **57**, 29–38, https://doi.org/10.1016/j.coldregions.2009.01.003.

Gautier, D.L., Bird, K.J., Charpentier, R.R., Grantz, A., Houseknecht, D.W., Klett, T.R., et al. (2009) Assessment of undiscovered oil and gas in the arctic. *Science*, **324**, 1175–1179, https://doi.org/10.1126/science.1169467.

Haas, C., Beckers, J., King, J., Silis, A., Stroeve, J., Wilkinson, J., et al. (2017) Ice and snow thickness variability and change in the high Arctic Ocean observed by in situ measurements. *Geophysical Research Letters*, **44**, 10,462–10,469, https://doi.org/10.1002/2017GL075434.

Haas, C. & Druckenmiller, M. (2009) Ice thickness and roughness measurements. In: *Field Techniques for Sea Ice Research*, 49–116, University of Alaska Press.

Haas, C., Gerland, S., Eicken, H. & Miller, H. (1997) Comparison of sea-ice thickness measurements under summer and winter conditions in the Arctic using a small

electromagnetic induction device. *Geophysics*, **62**, 749–757.

Haas, C., Hendricks, S., Eicken, H. & Herber, A. (2010) Synoptic airborne thickness surveys reveal state of Arctic sea ice cover. *Geophysical Research Letters*, **37**, https://doi.org/10.1029/2010gl042652.

Haas, C. & Jochmann, P. (2003) Continuous EM and ULS thickness profiling in support of ice force measurements. In: *Proceedings of the 17th International Conference on Port and Ocean Engineering under Arctic Conditions*, POAC '03, Trondheim, Norway (Eds. S. Loeset, B. Bonnemaire & M. Bjerkas), pp. 849–856. Department of Civil and Transport Engineering, Norwegian University of Science and Technology.

Haas, C., Langhorne, P.J., Rack, W., Leonard, G.H., Brett, G.M., Price, D., et al. (2021) Airborne mapping of the sub-ice platelet layer under fast ice in McMurdo Sound, Antarctica. *The Cryosphere*, **15**, 247–264, https://doi.org/10.5194/tc-15-247-2021.

Haas, C., Lobach, J., Hendricks, S., Rabenstein, L. & Pfaffling, A. (2009) Helicopter-borne measurements of sea ice thickness, using a small and lightweight, digital EM system. *Journal of Applied Geophysics*, **67**, 234–241, https://doi.org/10.1016/j.jappgeo.2008.05.005.

Haas, C., Pfaffling, A., Hendricks, S., Rabenstein, L., Etienne, J.-L. & Rigor, I. (2008) Reduced ice thickness in Arctic Transpolar Drift favors rapid ice retreat. *Geophysical Research Letters*, **35**, L17501, https://doi.org/10.1029/2008GL034457.

Hansen, E., Gerland, S., Granskog, M.A., Pavlova, O., Renner, A.H.H., Haapala, J., et al. (2013) Thinning of Arctic sea ice observed in Fram Strait: 1990–2011. *Journal of Geophysical Research: Oceans*, **118**, 5202–5221, https://doi.org/10.1002/jgrc.20393.

Hendricks, S., Paul, S., & Rinne, E. (2024a) ESA Sea Ice Climate Change Initiative (Sea_Ice_cci): Northern hemisphere sea ice thickness from the CryoSat-2 satellite on a monthly grid (L3C), v3.0. NERC EDS Centre for Environmental Data Analysis

Hendricks, S., Paul, S., & Rinne, E. (2024b) ESA Sea Ice Climate Change Initiative (Sea_Ice_cci): Southern hemisphere sea ice thickness from the CryoSat-2 satellite on a monthly grid (L3C), v3.0. NERC EDS Centre for Environmental Data AnalysisHibler, W.D. (1979) A dynamic thermodynamic sea ice model. *Journal of Physical Oceanography*, **9**, 815–846, https://doi.org/10.1175/1520-0485(1979)009<0815:adtsim>2.0.co;2.

Holland, M.M., Bitz, C.M., Hunke, E.C., Lipscomb, W.H. & Schramm, J.L. (2006) Influence of the sea ice thickness distribution on Polar climate in CCSM3. *Journal of Climate*, **19**, 2398–2414, https://doi.org/10.1175/jcli3751.1.

Hopkins, M.A. (1994) On the ridging of intact lead ice. *Journal of Geophysical Research*, **99**, 16351, https://doi.org/10.1029/94jc00996.

Hopkins, M.A. (1998) Four stages of pressure ridging. *Journal of Geophysical Research: Oceans*, **103**, 21883–21891, https://doi.org/10.1029/98jc01257.

Hopkins, M.A., Hibler, W.D. & Flato, G.M. (1991) On the numerical simulation of the sea ice ridging process. *Journal of Geophysical Research*, **96**, 4809, https://doi.org/10.1029/90jc02375.

Hopkins, M.A., Tuhkuri, J. & Lensu, M. (1999) Rafting and ridging of thin ice sheets. *Journal of Geophysical Research: Oceans*, **104**, 13605–13613, https://doi.org/10.1029/1999jc900031.

Hoppmann, M., Richter, M.E., Smith, I.J., Jendersie, S., Langhorne, P.J., Thomas, D.N., et al. (2020) Platelet ice, the Southern Ocean's hidden ice: a review. *Annals of Glaciology*, **61**, 341–368, https://doi.org/10.1017/aog.2020.54.

Hunkeler, P.A., Hoppmann, M., Hendricks, S., Kalscheuer, T. & Gerdes, R. (2016) A glimpse beneath Antarctic sea ice: platelet layer volume from multifrequency electromagnetic induction sounding. *Geophysical Research*

Letters, **43**, 222–231, https://doi.org/10.1002/2015GL065074.

Hutter, N. & Losch, M. (2020) Feature-based comparison of sea ice deformation in lead-permitting sea ice simulations. *The Cryosphere*, **14**, 93–113, https://doi.org/10.5194/tc-14-93-2020.

Hutter, N., Zampieri, L. & Losch, M. (2019) Leads and ridges in Arctic sea ice from RGPS data and a new tracking algorithm. *The Cryosphere*, **13**, 627–645, https://doi.org/10.5194/tc-13-627-2019.

Hutter, N.C., Bouchat, A., Dupont, F., Dukhovskoy, D.S., Koldunov, N.V., Lee, Y.J., et al. (2022) Sea Ice Rheology Experiment (SIREx): 2. Evaluating linear kinematic features in high-resolution sea ice simulations. *Journal of Geophysical Research: Oceans*, **127**, e2021JC017666, https://doi.org/10.1029/2021jc017666.

Hwang, B., Wilkinson, J., Maksym, T., Graber, H.C., Schweiger, A., Horvat, C., et al. (2017) Winter-to-summer transition of Arctic sea ice breakup and floe size distribution in the Beaufort Sea (Eds. J.W. Deming & J. Thomson). *Elementa: Science of the Anthropocene*, **5**, 40, https://doi.org/10.1525/elementa.232.

Itkin, P., Hendricks, S., Webster, M., von Albedyll, L., Arndt, S., Divine, D., et al. (2023) Sea ice and snow characteristics from year-long transects at the MOSAiC Central Observatory. *Elementa: Science of the Anthropocene*, **11**, 00048, https://doi.org/10.1525/elementa.2022.00048.

Itkin, P., Spreen, G., Hvidegaard, S.M., Skourup, H., Wilkinson, J., Gerland, S., et al. (2018) Contribution of deformation to sea ice mass balance: a case study from an N-ICE2015 storm. *Geophysical Research Letters*, **45**, 789–796, https://doi.org/10.1002/2017gl076056.

Jackson, K., Wilkinson, J., Maksym, T., Meldrum, D., Beckers, J., Haas, C., et al. (2013) A novel and low-cost sea ice mass balance buoy. *Journal of Atmospheric and Oceanic Technology*, **30**, 2676–2688, https://doi.org/10.1175/jtech-d-13-00058.1.

Jutila, A., Hendricks, S., Ricker, R., von Albedyll, L., Krumpen, T. & Haas, C. (2022a) Retrieval and parameterisation of sea-ice bulk density from airborne multi-sensor measurements. *The Cryosphere*, **16**, 259–275, https://doi.org/10.5194/tc-16-259-2022.

Jutila, A., King, J., Paden, J., Ricker, R., Hendricks, S., Polashenski, C., et al. (2022b) High-resolution snow depth on Arctic sea ice from low-altitude airborne microwave radar data. *IEEE Transactions on Geoscience and Remote Sensing*, **60**, 1–16, https://doi.org/10.1109/TGRS.2021.3063756.

Kacimi, S. & Kwok, R. (2020) The Antarctic sea ice cover from ICESat-2 and CryoSat-2: freeboard, snow depth, and ice thickness. *The Cryosphere*, **14**, 4453–4474, https://doi.org/10.5194/tc-14-4453-2020.

Kacimi, S. & Kwok, R. (2022) Arctic snow depth, ice thickness, and volume from ICESat-2 and CryoSat-2: 2018–2021. *Geophysical Research Letters*, **49**, https://doi.org/10.1029/2021gl097448.

Kacimi, S. & Kwok, R. (2024) Two decades of Arctic Sea-Ice thickness from satellite altimeters: retrieval approaches and record of changes (2003–2023). *Remote Sensing*, **16**, https://doi.org/10.3390/rs16162983.

Keen, A., Blockley, E., Bailey, D.A., Debernard, J.B., Bushuk, M., Delhaye, S., et al. (2021) An inter-comparison of the mass budget of the Arctic sea ice in CMIP6 models. *The Cryosphere*, **15**, 951–982, https://doi.org/10.5194/tc-15-951-2021.

Kern, M., Cullen, R., Berruti, B., Bouffard, J., Casal, T., Drinkwater, M.R., et al. (2020) The Copernicus Polar Ice and Snow Topography Altimeter (CRISTAL) high-priority candidate mission. *The Cryosphere*, **14**, 2235–2251, https://doi.org/10.5194/tc-14-2235-2020.

Khon, V.C., Mokhov, I.I., Latif, M., Semenov, V.A. & Park, W. (2009) Perspectives of Northern Sea Route and Northwest Passage in the twenty-first century. *Climatic Change*, **100**,

757–768, https://doi.org/10.1007/s10584-009-9683-2.

Koerner, R.M. (1973) The mass balance of the sea ice of the Arctic Ocean. *Journal of Glaciology*, **12**, 173–185, https://doi.org/10.3189/s0022143000032020.

Koo, Y., Lei, R., Cheng, Y., Cheng, B., Xie, H., Hoppmann, M., et al. (2021) Estimation of thermodynamic and dynamic contributions to sea ice growth in the Central Arctic using ICESat-2 and MOSAiC SIMBA buoy data. *Remote Sensing of Environment*, **267**, 112730, https://doi.org/10.1016/j.rse.2021.112730.

Kovacs, A. & Holladay, J.S. (1990) Sea-ice thickness measurement using a small airborne electromagnetic sounding system. *Geophysics*, **55**, 1327–1337, https://doi.org/10.1190/1.1442780.

Kovacs, A., Holladay, J.S. & Bergeron, C.J., Jr. (1995) The footprint/altitude ratio for helicopter electromagnetic sounding of sea-ice thickness: comparison of theoretical and field estimates. *Geophysics*, **60**, 374–380, https://doi.org/10.1190/1.1443773.

Krishfield, R.A., Proshutinsky, A., Tateyama, K., Williams, W.J., Carmack, E.C., McLaughlin, F.A., et al. (2014) Deterioration of perennial sea ice in the Beaufort Gyre from 2003 to 2012 and its impact on the oceanic freshwater cycle. *Journal of Geophysical Research: Oceans*, **119**, 1271–1305, https://doi.org/10.1002/2013JC008999.

Krumpen, T., Belter, H.J., Boetius, A., Damm, E., Haas, C., Hendricks, S., et al. (2019) Arctic warming interrupts the Transpolar Drift and affects long-range transport of sea ice and ice-rafted matter. *Scientific Reports*, **9**, 5459, https://doi.org/10.1038/s41598-019-41456-y.

Krumpen, T., von Albedyll, L., Bünger, H.J., Castellani, G., Hartmann, J., Helm, V., et al. (2025) Smoother sea ice with fewer pressure ridges in a more dynamic Arctic. *Nature Climate Change*, https://doi.org/10.1038/s41558-024-02199-5.

Kurtz, N.T., Farrell, S.L., Studinger, M., Galin, N., Harbeck, J.P., Lindsay, R., et al. (2013) Sea ice thickness, freeboard, and snow depth products from Operation IceBridge airborne data. *The Cryosphere*, **7**, 1035–1056, https://doi.org/10.5194/tc-7-1035-2013.

Kwok, R. (2006) Contrasts in sea ice deformation and production in the Arctic seasonal and perennial ice zones. *Journal of Geophysical Research*, **111**, C11S22, https://doi.org/10.1029/2005jc003246.

Kwok, R. (2018) Arctic sea ice thickness, volume, and multiyear ice coverage: losses and coupled variability (1958–2018). *Environmental Research Letters*, **13**, 105005, https://doi.org/10.1088/1748-9326/aae3ec.

Kwok, R. & Cunningham, G.F. (2016) Contributions of growth and deformation to monthly variability in sea ice thickness north of the coasts of Greenland and the Canadian Arctic Archipelago. *Geophysical Research Letters*, **43**, 8097–8105, https://doi.org/10.1002/2016gl069333.

Kwok, R., Kurtz, N.T., Brucker, L., Ivanoff, A., Newman, T., Farrell, S.L., et al. (2017) Intercomparison of snow depth retrievals over Arctic sea ice from radar data acquired by Operation IceBridge. *The Cryosphere*, **11**, 2571–2593, https://doi.org/10.5194/tc-11-2571-2017.

Kwok, R. & Maksym, T. (2014) Snow depth of the Weddell and Bellingshausen sea ice covers from IceBridge surveys in 2010 and 2011: an examination. *Journal of Geophysical Research: Oceans*, **119**, 4141–4167, https://doi.org/10.1002/2014JC009943.

Landy, J., Ehn, J., Shields, M. & Barber, D. (2014) Surface and melt pond evolution on landfast first-year sea ice in the Canadian Arctic Archipelago. *Journal of Geophysical Research: Oceans*, **119**, 3054–3075, https://doi.org/10.1002/2013jc009617.

Landy, J.C., Dawson, G.J., Tsamados, M., Bushuk, M., Stroeve, J.C., Howell, S.E.L., et al. (2022) A year-round satellite sea-ice

thickness record from CryoSat-2. *Nature*, **609**, 517–522, https://doi.org/10.1038/s41586-022-05058-5.

Langhorne, P.J., Haas, C., Price, D., Rack, W., Leonard, G.H., Brett, G.M., et al. (2023) Fast ice thickness distribution in the western Ross Sea in late spring. *Journal of Geophysical Research: Oceans*, **128**, e2022JC019459, https://doi.org/10.1029/2022JC019459.

Langhorne, P.J., Hughes, K.G., Gough, A.J., Smith, I.J., Williams, M.J.M., Robinson, N.J., et al. (2015) Observed platelet ice distributions in Antarctic sea ice: an index for ocean-ice shelf heat flux. *Geophysical Research Letters*, **42**, 5442–5451, https://doi.org/10.1002/2015GL064508.

Lavergne, T. & Down, E. (2023) A climate data record of year-round global sea-ice drift from the EUMETSAT Ocean and Sea Ice Satellite Application Facility (OSI SAF). *Earth System Science Data*, **15**, 5807–5834, https://doi.org/10.5194/essd-15-5807-2023.

Laxon, S., Peacock, N. & Smith, D. (2003) High interannual variability of sea ice thickness in the Arctic region. *Nature*, **425**, 947–950, https://doi.org/10.1038/nature02050.

Lei, R., Gui, D., Hutchings, J.K., Heil, P. & Li, N. (2020) Annual cycles of sea ice motion and deformation derived from buoy measurements in the western Arctic ocean over two ice seasons. *Journal of Geophysical Research: Oceans*, **125**, e2019JC015310, https://doi.org/10.1029/2019jc015310.

Lindsay, R. & Schweiger, A. (2015) Arctic sea ice thickness loss determined using subsurface, aircraft, and satellite observations. *The Cryosphere*, **9**, 269–283, https://doi.org/10.5194/tc-9-269-2015.

Lipscomb, W.H., Hunke, E.C., Maslowski, W. & Jakacki, J. (2007) Ridging, strength, and stability in high-resolution sea ice models. *Journal of Geophysical Research*, **112**, C03S91, https://doi.org/10.1029/2005JC003355.

Lytle, V.I. & Ackley, S.F. (1996) Heat flux through sea ice in the western Weddell Sea: convective and conductive transfer processes. *Journal of Geophysical Research: Oceans*, **101**, 8853–8868, https://doi.org/10.1029/95JC03675.

MacGregor, J.A., Boisvert, L.N., Medley, B., Petty, A.A., Harbeck, J.P., Bell, R.E., et al. (2021) The scientific legacy of NASA's Operation IceBridge. *Reviews of Geophysics*, **59**, e2020RG000712, https://doi.org/10.1029/2020RG000712.

Magruder, L.A., Brunt, K.M. & Alonzo, M. (2020) Early ICESat-2 on-orbit Geolocation Validation Using Ground-Based Corner Cube Retro-Reflectors. *Remote Sensing*, **12**, 10.3390/rs12213653

Mahoney, A.R., Eicken, H., Fukamachi, Y., Ohshima, K.I., Simizu, D., Kambhamettu, C., et al. (2015) Taking a look at both sides of the ice: comparison of ice thickness and drift speed as observed from moored, airborne and shore-based instruments near Barrow, Alaska. *Annals of Glaciology*, **56**, 363–372, https://doi.org/10.3189/2015AoG69A565.

Maksym, T., Stammerjohn, S.E., Ackley, S. & Massom, R. (2012) Antarctic sea ice: a polar opposite? *Oceanography*, **25**, 140–151.

Massom, R.A., Eicken, H., Hass, C., Jeffries, M.O., Drinkwater, M.R., Sturm, M., et al. (2001) Snow on Antarctic sea ice. *Reviews of Geophysics*, **39**, 413–445, https://doi.org/10.1029/2000RG000085.

Massonnet, F., Barthélemy, A., Worou, K., Fichefet, T., Vancoppenolle, M., Rousset, C., et al. (2019) On the discretization of the ice thickness distribution in the NEMO3.6-LIM3 global ocean–sea ice model. *Geoscientific Model Development*, **12**, 3745–3758, https://doi.org/10.5194/gmd-12-3745-2019.

Massonnet, F., Vancoppenolle, M., Goosse, H., Docquier, D., Fichefet, T. & Blanchard-Wrigglesworth, E. (2018) Arctic sea-ice change tied to its mean state through thermodynamic processes. *Nature Climate Change*, **8**, 599–603, https://doi.org/10.1038/s41558-018-0204-z.

Maykut, G.A. (1986) The surface heat and mass balance. In: *The Geophysics of Sea Ice* (Ed. N. Untersteiner), pp. 395–463. Springer, Boston,

MA, https://doi.org/10.1007/978-1-4899-5352-0_6.

Mchedlishvili, A., Lüpkes, C., Petty, A., Tsamados, M. & Spreen, G. (2023) New estimates of pan-Arctic sea ice–atmosphere neutral drag coefficients from ICESat-2 elevation data. *The Cryosphere*, **17**, 4103–4131, https://doi.org/10.5194/tc-17-4103-2023.

Mehlmann, C., Capodaglio, G. & Danilov, S. (2023) Simulating sea-ice deformation in viscous-plastic sea-ice models with CD-Grids. *Journal of Advances in Modeling Earth Systems*, **15**, e2023MS003696, https://doi.org/10.1029/2023MS003696.

Mehlmann, C., Danilov, S., Losch, M., Lemieux, J.F., Hutter, N., Richter, T., et al. (2021) Simulating linear kinematic features in viscous-plastic sea ice models on quadrilateral and triangular grids with different variable staggering. *Journal of Advances in Modeling Earth Systems*, **13**, e2021MS002523, https://doi.org/10.1029/2021MS002523.

Meier, W. & Haas, C. (2011) Changes in the physical state of sea ice. In: *Snow, Water, Ice and Permafrost in the Arctic (SWIPA): Climate Change and the Cryosphere*, xii + 538 pp., 9–4 to 9–18. Arctic Monitoring and Assessment Programme (AMAP), Oslo, Norway.

Meier, W.N., Hovelsrud, G.K., van Oort, B.E.H., Key, J.R., Kovacs, K.M., Michel, C., et al. (2014) Arctic sea ice in transformation: a review of recent observed changes and impacts on biology and human activity. *Reviews of Geophysics*, **52**, 185–217, https://doi.org/10.1002/2013rg000431.

Melling, H. & Riedel, D.A. (1995) The underside topography of sea ice over the continental shelf of the Beaufort Sea in the winter of 1990. *Journal of Geophysical Research: Oceans*, **100**, 13641–13653, https://doi.org/10.1029/95JC00309

Melling, H. & Riedel, D. (2004) Draft and movement of pack ice in the Beaufort Sea: a time-series presentation April 1990-August 1999. *Canadian Technical Report of Hydrography and Ocean Sciences*, **238**, https://waves-vagues.dfo-mpo.gc.ca/Library/282300.pdf.

Melling, H., Riedel, D.A. & Gedalof, Z. (2005) Trends in the draft and extent of seasonal pack ice, Canadian Beaufort Sea. *Geophysical Research Letters*, **32**, https://doi.org/10.1029/2005GL024483.

Metzger, A.T., Mahoney, A.R. & Roberts, A.F. (2021) The average shape of sea ice ridge keels. *Geophysical Research Letters*, **48**, e2021GL095100, https://doi.org/10.1029/2021GL095100.

Mioduszewski, J.R., Vavrus, S., Wang, M., Holland, M. & Landrum, L. (2019) Past and future interannual variability in Arctic sea ice in coupled climate models. *The Cryosphere*, **13**, 113–124, https://doi.org/10.5194/tc-13-113-2019.

Moon, T., Thoman, R., Druckenmiller, M., Ahmasuk, B., Backensto, S. A., Ballinger, T. J., et al. (2023) The Arctic. *Bulletin of the American Meteorological Society*, **104**, S271–S321.

Muchow, M. & Polojärvi, A. (2024) Three-dimensional discrete element simulations on pressure ridge formation. *EGUsphere*, **2024**, 1–15, https://doi.org/10.5194/egusphere-2024-831.

Muchow, M., Schmitt, A.U. & Kaleschke, L. (2021) A lead-width distribution for Antarctic sea ice: a case study for the Weddell Sea with high-resolution Sentinel-2 images. *The Cryosphere*, **15**, 4527–4537, https://doi.org/10.5194/tc-15-4527-2021.

Neudert, M., Arndt, S., Hendricks, S., Hoppmann, M., Schulze, M. & Haas, C. (2024) Improved sub-ice platelet layer mapping with multi-frequency EM induction sounding. *Journal of Applied Geophysics*, **230**, 105540, https://doi.org/10.1016/j.jappgeo.2024.105540.

Niederdrenk, A.L. & Notz, D. (2018) Arctic sea ice in a 1.5°C warmer world. *Geophysical Research Letters*, **45**, 1963–1971, https://doi.org/10.1002/2017gl076159.

Notz, D. (2009) The future of ice sheets and sea ice: between reversible retreat and unstoppable loss. *Proceedings of the National Academy of Sciences*, **106**, 20590–20595, https://doi.org/10.1073/pnas.0902356106.

Panzer, B., Gomez-Garcia, D., Leuschen, C., Paden, J., Rodriguez-Morales, F., Patel, A., et al. (2013) An ultra-wideband, microwave radar for measuring snow thickness on sea ice and mapping near-surface internal layers in polar firn. *Journal of Glaciology*, **59**, 244–254, https://doi.org/10.3189/2013JoG12J128.

Paul, S., Hendricks, S., Ricker, R., Kern, S. & Rinne, E. (2018) Empirical parametrization of Envisat freeboard retrieval of Arctic and Antarctic sea ice based on CryoSat-2: progress in the ESA Climate Change Initiative. *The Cryosphere*, **12**, 2437–2460, https://doi.org/10.5194/tc-12-2437-2018.

Perovich, D., Meier, W., Tschudi, M., Hendricks, S., Petty, A.A., Divine, D., et al. (2020) Arctic Report Card 2020: Sea Ice, https://doi.org/10.25923/N170-9H57.

Perovich, D., Raphael, I., Moore, R., Clemens-Sewall, D., Lei, R., Sledd, A., et al. (2023) Sea ice heat and mass balance measurements from four autonomous buoys during the MOSAiC drift campaign. *Elementa: Science of the Anthropocene*, **11**, 00017, https://doi.org/10.1525/elementa.2023.00017.

Perovich, D.K., Grenfell, T.C., Richter-Menge, J.A., Light, B., Tucker III, W.B. & Eicken, H. (2003) Thin and thinner: sea ice mass balance measurements during SHEBA. *Journal of Geophysical Research*, **108**, 8050, https://doi.org/10.1029/2001jc001079.

Perovich, D.K., Richter-Menge, J.A. & Tucker, W.B. (2001) Seasonal changes in Arctic sea-ice morphology. *Annals of Glaciology*, **33**, 171–176, https://doi.org/10.3189/172756401781818716.

Petrich, C. & Eicken, H. (2017) Overview of sea ice growth and properties. In: *Sea Ice*, pp. 1–41, WILEY. https://doi.org/10.1002/9781118778371.ch1.

Petty, A.A., Tsamados, M.C. & Kurtz, N.T. (2017) Atmospheric form drag coefficients over Arctic sea ice using remotely sensed ice topography data, spring 2009–2015. *Journal of Geophysical Research: Earth Surface*, **122**, 1472–1490, https://doi.org/10.1002/2017jf004209.

Petty, A.A., Tsamados, M.C., Kurtz, N.T., Farrell, S.L., Newman, T., Harbeck, J.P., et al. (2016) Characterizing Arctic sea ice topography using high-resolution IceBridge data. *The Cryosphere*, **10**, 1161–1179, https://doi.org/10.5194/tc-10-1161-2016.

Pfaffling, A., Haas, C. & Reid, J.E. (2007) A Direct helicopter EM — sea-ice thickness inversion assessed with synthetic and field data. *Geophysics*, **72**, F127–F137, https://doi.org/10.1190/1.2732551.

Polashenski, C., Perovich, D. & Courville, Z. (2012) The mechanisms of sea ice melt pond formation and evolution. *Journal of Geophysical Research: Oceans*, **117**, https://doi.org/10.1029/2011JC007231.

Polyakov, I.V., Ingvaldsen, R.B., Pnyushkov, A.V., Bhatt, U.S., Francis, J.A., Janout, M., et al. (2023) Fluctuating Atlantic inflows modulate Arctic atlantification. *Science*, **381**, 972–979, https://doi.org/10.1126/science.adh5158.

Polyakov, I.V., Pnyushkov, A.V., Alkire, M.B., Ashik, I.M., Baumann, T.M., Carmack, E.C., et al. (2017) Greater role for Atlantic inflows on sea-ice loss in the Eurasian Basin of the Arctic Ocean. *Science*, **356**, 285–291, https://doi.org/10.1126/science.aai8204.

Post, E., Bhatt, U.S., Bitz, C.M., Brodie, J.F., Fulton, T.L., Hebblewhite, M., Kerby, J., et al. (2013) Ecological consequences of sea-ice decline. *Science*, **341**, 519–524, https://doi.org/10.1126/science.1235225.

Price, D., Rack, W., Langhorne, P.J., Haas, C., Leonard, G. & Barnsdale, K. (2014) The sub-ice platelet layer and its influence on freeboard to thickness conversion of Antarctic sea ice. *The Cryosphere*, **8**, 1031–1039, https://doi.org/10.5194/tc-8-1031-2014.

Purich, A. & Doddridge, E.W. (2023) Record low Antarctic sea ice coverage indicates a new sea ice state. *Communications Earth & Environment*, **4**, 314, https://doi.org/10.1038/s43247-023-00961-9.

Rabenstein, L., Hendricks, S., Martin, T., Pfaffhuber, A. & Haas, C. (2010) Thickness and surface-properties of different sea-ice regimes within the Arctic Trans Polar Drift: data from summers 2001, 2004 and 2007. *Journal of Geophysical Research*, **115**, C12059, https://doi.org/10.1029/2009jc005846.

Rack, W., Price, D., Haas, C., Langhorne, P.J. & Leonard, G.H. (2021) Sea ice thickness in the Western Ross Sea. *Geophysical Research Letters*, **48**, e2020GL090866, https://doi.org/10.1029/2020gl090866.

Rampal, P., Bouillon, S., Ólason, E. & Morlighem, M. (2016) neXtSIM: a new Lagrangian sea ice model. *The Cryosphere*, **10**, 1055–1073, https://doi.org/10.5194/tc-10-1055-2016.

Reid, J.E., Pfaffling, A. & Vrbancich, J. (2006) Airborne electromagnetic footprints in 1D earths. *Geophysics*, **71**, G63–G72, https://doi.org/10.1190/1.2187756.

Reiser, F., Willmes, S. & Heinemann, G. (2020) A new algorithm for daily sea ice lead identification in the Arctic and Antarctic winter from thermal-infrared satellite imagery. *Remote Sensing*, **12**, 1957, https://doi.org/10.3390/rs12121957.

Richter-Menge, J.A., Perovich, D.K., Elder, B.C., Claffey, K., Rigor, I. & Ortmeyer, M. (2006) Ice mass-balance buoys: a tool for measuring and attributing changes in the thickness of the Arctic sea-ice cover. *Annals of Glaciology*, **44**, 205–210, https://doi.org/10.3189/172756406781811727.

Ricker, R., Fons, S., Jutila, A., Hutter, N., Duncan, K., Farrell, S.L., et al. (2023) Linking scales of sea ice surface topography: evaluation of ICESat-2 measurements with coincident helicopter laser scanning during MOSAiC. *The Cryosphere*, **17**, 1411–1429, https://doi.org/10.5194/tc-17-1411-2023.

Ricker, R., Hendricks, S. & Beckers, J.F. (2016) The impact of geophysical corrections on sea-ice freeboard retrieved from satellite altimetry. *Remote Sensing*, **8**, https://doi.org/10.3390/rs8040317.

Ricker, R., Hendricks, S., Kaleschke, L., Tian-Kunze, X., King, J. & Haas, C. (2017) A weekly Arctic sea-ice thickness data record from merged CryoSat-2 and SMOS satellite data. *The Cryosphere*, **11**, 1607–1623, https://doi.org/10.5194/tc-11-1607-2017.

Ricker, R., Kauker, F., Schweiger, A., Hendricks, S., Zhang, J. & Paul, S. (2021) Evidence for an increasing role of ocean heat in Arctic winter sea ice growth. *Journal of Climate*, **34**, 5215–5227, https://doi.org/10.1175/jcli-d-20-0848.1.

Ringeisen, D., Hutter, N. & von Albedyll, L. (2023) Deformation lines in Arctic sea ice: intersection angle distribution and mechanical properties. *The Cryosphere*, **17**, 4047–4061, https://doi.org/10.5194/tc-17-4047-2023.

Roberts, A.F., Hunke, E.C., Kamal, S.M., Lipscomb, W.H., Horvat, C. & Maslowski, W. (2019) A variational method for sea ice ridging in earth system models. *Journal of Advances in Modeling Earth Systems*, **11**, 771–805, https://doi.org/10.1029/2018ms001395.

Rösel, A., Itkin, P., King, J., Divine, D., Wang, C., Granskog, M.A., et al. (2018) Thin sea ice, thick snow, and widespread negative freeboard observed during N-ICE2015 north of Svalbard. *Journal of Geophysical Research: Oceans*, **123**, 1156–1176, https://doi.org/10.1002/2017jc012865.

Rothrock, D.A. (1975) The energetics of the plastic deformation of pack ice by ridging. *Journal of Geophysical Research*, 4514–4519.

Rothrock, D.A., Percival, D.B. & Wensnahan, M. (2008) The decline in arctic sea-ice thickness: separating the spatial, annual, and interannual variability in a quarter century of submarine data. *Journal of Geophysical Research*, **113**, C05003, https://doi.org/10.1029/2007jc004252.

Rothrock, D.A. & Wensnahan, M. (2007) The accuracy of sea ice drafts measured from U.S. Navy Submarines. *Journal of Atmospheric and Oceanic Technology*, **24**, 1936–1949, https://doi.org/10.1175/JTECH2097.1.

Rothrock, D.A., Yu, Y. & Maykut, G.A. (1999) Thinning of the Arctic sea-ice cover. *Geophysical Research Letters*, **26**, 3469–3472, https://doi.org/10.1029/1999gl010863.

Saldern, C. von, Haas, C. & Dierking, W. (2006) Parameterization of Arctic sea-ice surface roughness for application in ice type classification. *Annals of Glaciology*, **44**, 224–230, https://doi.org/10.3189/172756406781811411.

Salganik, E., Lange, B.A., Katlein, C., Matero, I., Anhaus, P., Muilwijk, M., et al. (2023) Observations of preferential summer melt of Arctic sea-ice ridge keels from repeated multibeam sonar surveys. *The Cryosphere*, **17**, 4873–4887, https://doi.org/10.5194/tc-17-4873-2023.

Schweiger, A.J., Steele, M., Zhang, J., Moore, G.W.K. & Laidre, K.L. (2021) Accelerated sea ice loss in the Wandel Sea points to a change in the Arctic's Last Ice Area. *Communications Earth & Environment*, **2**, https://doi.org/10.1038/s43247-021-00197-5.

Smith, M.M., von Albedyll, L., Raphael, I.A., Lange, B.A., Matero, I., Salganik, E., et al. (2022) Quantifying false bottoms and under-ice meltwater layers beneath Arctic summer sea ice with fine-scale observations. *Elementa: Science of the Anthropocene*, **10**, https://doi.org/10.1525/elementa.2021.000116.

Stroeve, J. & Notz, D. (2018) Changing state of Arctic sea ice across all seasons. *Environmental Research Letters*, **13**, 103001, https://doi.org/10.1088/1748-9326/aade56.

Stroeve, J.C., Schroder, D., Tsamados, M. & Feltham, D. (2018) Warm winter, thin ice? *The Cryosphere*, **12**, 1791–1809, https://doi.org/10.5194/tc-12-1791-2018.

Sumata, H., de Steur, L., Divine, D.V., Granskog, M.A. & Gerland, S. (2023) Regime shift in Arctic Ocean sea ice thickness. *Nature*, **615**, 443–449, https://doi.org/10.1038/s41586-022-05686-x.

Tan, B., Li, Z., Lu, P., Haas, C. & Nicolaus, M. (2012) Morphology of sea ice pressure ridges in the northwestern Weddell Sea in winter. *Journal of Geophysical Research: Oceans*, **117**, https://doi.org/10.1029/2011JC007800.

Thorndike, A.S. (1992a) A toy model linking atmospheric thermal radiation and sea ice growth. *Journal of Geophysical Research*, **97**, 9401–9410, https://doi.org/10.1029/92jc00695.

Thorndike, A.S. (1992b) Estimates of sea ice thickness distribution using observations and theory. *Journal of Geophysical Research*, **97**, 12601–12605, https://doi.org/10.1029/92jc01199.

Thorndike, A.S., Rothrock, D.A., Maykut, G.A. & Colony, R. (1975) The thickness distribution of sea ice. *Journal of Geophysical Research*, **80**, 4501–4513, https://doi.org/10.1029/jc080i033p04501.

Tietsche, S., Notz, D., Jungclaus, J.H. & Marotzke, J. (2011) Recovery mechanisms of Arctic summer sea ice. *Geophysical Research Letters*, **38**, https://doi.org/10.1029/2010GL045698.

Tilling, R.L., Ridout, A. & Shepherd, A. (2018) Estimating Arctic sea ice thickness and volume using CryoSat-2 radar altimeter data. *Advances in Space Research*, **62**, 1203–1225, https://doi.org/10.1016/j.asr.2017.10.051.

Tschudi, M., Stroeve, J. & Stewart, J. (2016) Relating the age of Arctic sea ice to its thickness, as measured during NASA's ICESat and IceBridge campaigns. *Remote Sensing*, **8**, 457, https://doi.org/10.3390/rs8060457.

Tuhkuri, J. & Lensu, M. (2002) Laboratory tests on ridging and rafting of ice sheets. *Journal of Geophysical Research: Oceans*, **107**, https://doi.org/10.1029/2001JC000848.

Turner, J., Hosking, J.S., Bracegirdle, T.J., Marshall, G.J. & Phillips, T. (2015) Recent changes in Antarctic Sea Ice. *Philosophical Transactions of the Royal Society A: Mathematical, Physical and Engineering*

Sciences, **373**, 20140163, https://doi.org/10.1098/rsta.2014.0163.

Ungermann, M., Tremblay, L.B., Martin, T. & Losch, M. (2017) Impact of the ice strength formulation on the performance of a sea ice thickness distribution model in the Arctic. *Journal of Geophysical Research: Oceans*, **122**, 2090–2107, https://doi.org/10.1002/2016jc012128.

Vinje, T., Nordlund, N. & Kvambekk, Å. (1998) Monitoring ice thickness in Fram Strait. *Journal of Geophysical Research: Oceans*, **103**, 10437–10449, https://doi.org/10.1029/97jc03360.

von Albedyll, L., Haas, C. & Dierking, W. (2021) Linking sea ice deformation to ice thickness redistribution using high-resolution satellite and airborne observations. *The Cryosphere*, **15**, 2167–2186, https://doi.org/10.5194/tc-15-2167-2021.

von Albedyll, L., Hendricks, S., Grodofzig, R., Krumpen, T., Arndt, S., Belter, H.J., et al. (2022) Thermodynamic and dynamic contributions to seasonal Arctic sea ice thickness distributions from airborne observations. *Elementa: Science of the Anthropocene*, **10**, https://doi.org/10.1525/elementa.2021.00074.

von Albedyll, L., Hendricks, S., Hutter, N., Murashkin, D., Kaleschke, L., Willmes, S., et al. (2024) Lead fractions from SAR-derived sea ice divergence during MOSAiC. *The Cryosphere*, **18**, 1259–1285, https://doi.org/10.5194/tc-18-1259-2024.

Wadhams, P. (1994) Sea ice thickness changes and their relation to climate. In: *The Polar Oceans and Their Role in Shaping the Global Environment*, pp. 337–361. American Geophysical Union, https://doi.org/10.1029/GM085p0337.

Wadhams, P. (2000) *Ice in the Ocean*. Gordon and Breach Science Publishers, London, UK. ISBN: 90-5699-296-1.

Wadhams, P. & Davy, T. (1986) On the spacing and draft distributions for pressure ridge keels. *Journal of Geophysical Research*, **91**, 10697–10708, https://doi.org/10.1029/jc091ic09p10697.

Wadhams, P. & Horne, R.J. (1980) An analysis of ice profiles obtained by submarine sonar in the beaufort sea. *Journal of Glaciology*, **25**, 401–424, https://doi.org/10.3189/s0022143000015264.

Wang, Q., Danilov, S., Jung, T., Kaleschke, L. & Wernecke, A. (2016) Sea ice leads in the Arctic Ocean: Model assessment, interannual variability and trends. *Geophysical Research Letters*, **43**, 7019–7027, https://doi.org/10.1002/2016gl068696.

Wang, Q., Ricker, R. & Mu, L. (2021) Arctic sea ice decline preconditions events of anomalously low sea ice volume export through fram strait in the early 21st century. *Journal of Geophysical Research: Oceans*, **126**, https://doi.org/10.1029/2020jc016607.

Warren, S.G., Rigor, I.G., Untersteiner, N., Radionov, V.F., Bryazgin, N.N., Aleksandrov, Y.I., et al. (1999) Snow depth on Arctic Sea Ice. *Journal of Climate*, **12**, 1814–1829, https://doi.org/10.1175/1520-0442(1999)012<1814:sdoasi>2.0.co;2.

Webster, M., Gerland, S., Holland, M., Hunke, E., Kwok, R., Lecomte, O., et al. (2018) Snow in the changing sea-ice systems. *Nature Climate Change*, **8**, 946–953, https://doi.org/10.1038/s41558-018-0286-7.

Williams, G., Maksym, T., Wilkinson, J., Kunz, C., Murphy, C., Kimball, P., et al. (2015) Thick and deformed Antarctic sea ice mapped with autonomous underwater vehicles. *Nature Geoscience*, **8**, 61–67, https://doi.org/10.1038/ngeo2299.

Willmes, S. & Heinemann, G. (2016) Sea-Ice Wintertime lead frequencies and regional characteristics in the Arctic, 2003–2015. *Remote Sensing*, **8**, 4, https://doi.org/10.3390/rs8010004.

Worby, A.P., Geiger, C.A., Paget, M.J., Van Woert, M.L., Ackley, S.F. & DeLiberty, T.L. (2008) Thickness distribution of Antarctic sea ice. *Journal of Geophysical Research: Oceans*, **113**, https://doi.org/10.1029/2007JC004254.

Worby, A.P., Jeffries, M.O., Weeks, W.F., Morris, K. & Jaña, R. (1996) The thickness distribution of sea ice and snow cover during late winter in the Bellingshausen and Amundsen Seas, Antarctica. *Journal of Geophysical Research: Oceans*, **101**, 28441–28455, https://doi.org/10.1029/96JC02737.